

**AD-A276 554**



**NRL/FR/5640--94-9704**

## **Methods for SBS Threshold Reduction**

**A. M. SCOTT**

*Defense Research Agency  
Malvern, Worcestershire WR14 3PS, U.K.*

**W. T. WHITNEY**

*Laser Physics Branch  
Optical Sciences Division*

**M. T. DUIGNAN**

*Potomac Photonics, Inc.  
4445 Nicole Drive  
Lanham, MD 20706*

**DTIC**  
**ELECTE**  
**MAR 08 1994**  
**S E D**

**94-07459**



**January 30, 1994**

**DTIC**

**94**

**7**

Approved for public release; distribution unlimited.

# REPORT DOCUMENTATION PAGE

Form Approved  
OMB No. 0704-0188

Public reporting burden for this collection of information is estimated to average 1 hour per response, including the time for reviewing instructions, searching existing data sources, gathering and maintaining the data needed, and completing and reviewing the collection of information. Send comments regarding this burden estimate or any other aspect of this collection of information, including suggestions for reducing this burden, to Washington Headquarters Services, Directorate for Information Operations and Reports, 1215 Jefferson Davis Highway, Suite 1204, Arlington, VA 22202-4302, and to the Office of Management and Budget, Paperwork Reduction Project (0704-0188), Washington, DC 20503.

1. AGENCY USE ONLY (Leave Blank)		2. REPORT DATE January 30, 1994		3. REPORT TYPE AND DATES COVERED Final Report, March-December 1992	
4. TITLE AND SUBTITLE Methods for SBS Threshold Reduction				5. FUNDING NUMBERS ONR - 63217C-BMD WU - DN380-002	
6. AUTHOR(S) A. M. Scott,* W. T. Whitney, and M. T. Duignan**					
7. PERFORMING ORGANIZATION NAME(S) AND ADDRESS(ES) Naval Research Laboratory Washington, DC 20375-5320				8. PERFORMING ORGANIZATION REPORT NUMBER NRL/FR/5640-94-9704	
9. SPONSORING/MONITORING AGENCY NAME(S) AND ADDRESS(ES) Strategic Defense Initiative Office Washington, DC 20301				10. SPONSORING/MONITORING AGENCY REPORT NUMBER	
11. SUPPLEMENTARY NOTES * Defense Research Agency, Malvern, Worcestershire WR14 3PS, U.K. **Potomac Photonics, Inc., 4445 Nicole Drive, Lanham, MD 20706					
12a. DISTRIBUTION/AVAILABILITY STATEMENT Approved for public release; distribution unlimited.				12b. DISTRIBUTION CODE	
13. ABSTRACT (Maximum 200 words)  We have investigated methods for reducing the threshold for stimulated Brillouin scattering (SBS) using a frequency-narrowed Cr,Tm,Ho:YAG laser operating at 2.12 $\mu$ m. The SBS medium was carbon disulfide. Single-focus SBS and threshold reduction by using two foci, a loop, and a ring have been demonstrated. Theories for the loop-SBS and the ring-SBS geometries have been developed and compared with experimental results. Backscatter power, energy, and conjugate fidelity data are presented.					
14. SUBJECT TERMS Stimulated Brillouin scattering    Infrared lasers Phase conjugation Threshold reduction				15. NUMBER OF PAGES 59	
				16. PRICE CODE	
17. SECURITY CLASSIFICATION OF REPORT UNCLASSIFIED	18. SECURITY CLASSIFICATION OF THIS PAGE UNCLASSIFIED	19. SECURITY CLASSIFICATION OF ABSTRACT UNCLASSIFIED	20. LIMITATION OF ABSTRACT UL		

NSN 7540-01-280-5500

Standard Form 298 (Rev. 2-89)  
Prescribed by ANSI Std Z39-18  
298-102

## CONTENTS

EXECUTIVE SUMMARY .....	E-1
INTRODUCTION .....	1
REVIEW OF THE LOOP SCHEME .....	2
REVIEW OF THE RING SBS SCHEME .....	5
THEORY OF THE LOOP-SBS INTERACTION .....	5
PHASE CONJUGATION BY STIMULATED BRILLOUIN SCATTERING .....	8
LOOP EXPERIMENTS .....	22
THEORY OF THE RING-SBS SCHEME .....	38
RING EXPERIMENTS .....	43
CONCLUSIONS .....	50
REFERENCES .....	51

Accession For	
NTIS CRA&I	<input checked="" type="checkbox"/>
DTIC TAB	<input checked="" type="checkbox"/>
Unannounced	<input type="checkbox"/>
Justification .....	
By .....	
Distribution /	
Availability Codes	
Dist	Avail and/or Special
<b>A-1</b>	

## EXECUTIVE SUMMARY

This study has investigated methods of SBS threshold reduction for long pulse and quasi-cw lasers. Two SBS threshold reduction techniques were studied: the so-called "loop" and "ring" schemes. These techniques have also been investigated recently at TRW and at Imperial College, London.

This study was carried out by using a Cr,Tm,Ho:YAG laser source and an approximately 2-m path length ring or loop, with CS<sub>2</sub> as the active medium. We developed a theoretical model for the transient and steady state behavior of the loop and ring systems, taking into account geometrical aspects such as the role of overlapping Gaussian beams and gain enhancement resulting from speckle inhomogeneity. We then tested the theory and characterized the performance of the two systems.

We identified one of the key parameters in these ring and loop schemes as the ratio of longitudinal mode spacing to Brillouin bandwidth. In our experiments this parameter had a value of ~13. This is closer to the ratio that will apply to the planned APEX experiments than has been the case in experiments carried out elsewhere. APEX is an experiment being conducted at TRW under a contract with NRL to demonstrate continuous wave optical phase conjugation with a high-power chemical laser.

The loop and ring schemes were investigated experimentally by using a new compact arrangement in which the loop or ring was formed with two lenses, a high reflectivity mirror and a second mirror, or beamsplitter. This new arrangement was more compact and simpler to align than the conventional scheme, but it was equivalent for studying the physics of the two schemes.

The transient and steady state behavior was studied for each scheme, and the beam quality was investigated for both unaberrated and aberrated beams. The transient regime was characterized by measuring the "onset energy," the amount of energy incident on the cell before SBS starts. This was found to be relatively constant, irrespective of whether we were close to threshold or well above threshold. The steady state regime was characterized by the power transmitted through the loop or ring (usually taken to be the threshold power), and again this was usually constant during a pulse. The loop and ring data could be directly compared with conventional single-focus SBS and two-focus SBS.

In the case of the loop, the onset energy was 1.5 to 2 mJ and the threshold power was 7 kW. This compares with values of 4 mJ and 22 kW for single-focus SBS and 3 mJ and 15 kW for two-focus SBS.

There was some shot-to-shot variation in the loop onset energy but little variation in the steady state power threshold. For certain loop lengths the steady state behavior was constant and reproducible, and at other lengths (differing by a few cm) the transmitted power oscillated with a 50-ns period. This was due to longitudinal mode effects and was consistent with theory.

When optimized, the amount of threshold reduction of the loop was close to the value calculated from theory, giving support for the theory's validity. Similarly, the value of the onset energy was consistent with theoretical calculations.

When the input beam was diffraction limited, the loop produced a beam with higher fidelity than conventional SBS, with a Gaussian profile in the near and far field. Beam quality was also measured with a severely aberrated beam. When the aberrator was double passed by a conventional mirror, the beam was at least 5 times diffraction limited, with a complex speckle pattern in the far field. The loop scheme

produced a backscattered beam with 80% of the far-field energy in a Gaussian lobe close to the divergence of the unaberrated input beam. The remaining 20% of the energy was in a highly divergent "halo." The overall fidelity was approximately 60%.

For geometrical reasons, the ring scheme was set to be 2-m long, and the laser cavity was realigned so that its round-trip transit time matched the transit time of the ring. The ring had an onset energy of 1.8 mJ and a threshold power of 3.5 kW, compared with 5.5 mJ and 23 kW for single-focus SBS and 4 mJ and 15 kW for two-focus SBS, measured at the same time.

There were large shot-to-shot fluctuations in the power threshold, with the threshold sometimes a factor 3 to 5 greater than the minimum observed value. Care was taken to eliminate factors such as changes in the laser's spectrum or other characteristics. The phenomenon was attributed to sub-wavelength shot-to-shot variations in the length of the ring, which led to variations in the power threshold. The beam quality studies gave results almost identical with those observed for the loop.

A theory was developed for the ring to include longitudinal mode pulling. This phenomenon causes the radiation in the ring to be detuned from the Brillouin-shifted frequency. The maximum possible detuning depends on the transmission around the ring and the ratio of longitudinal mode spacing to Brillouin linewidth. In our case, this was 1.7 Brillouin linewidths. The theory showed that this detuning would cause the threshold to increase by a factor 4 compared with the case of zero detuning, which is consistent with our experimental results.

Recent observations by other workers have shown less variation in the transmitted power than predicted by our theory; they also showed that if aberrations were present in the ring, threshold reduction still took place.

A "ring" has all the attributes of a "loop" and the extra attribute that the pump and Stokes radiation are assumed to reproduce their spatial structure after each round trip. This one assumption leads to all the differences in the mathematical models for the two schemes. It is clear that this assumption is not valid if there are aberrations in the ring. These aberrations can either be inserted deliberately or the result of many components with imperfections in the beam path. When these aberrations break the symmetry of the ring, it will behave as a "loop," i.e., a separate four-wave mixing grating will appear. This grating is spatially identical to the conventional SBS grating in a true ring.

It is possible that other workers' experiments benefited from this phenomenon. The theoretical threshold of a loop is within a factor two of a ring, but the loop threshold is insensitive to small changes in cavity length or to aberrations in the loop. In contrast, a ring is equivalent to a laser resonator with a very narrow gain bandwidth and will have an output field best described by spatial modes. These will be greatly affected by aberrations, and the cavity's threshold depends on the precise cavity length.

If fluctuations in threshold power are observed in the APEX experiments, two possible solutions are suggested. An aberrator may be inserted in the ring to make it behave as a loop. If this approach fails, the length of the ring may be precisely controlled, for example, by using a servo loop to minimize the SBS threshold.

## METHODS FOR SBS THRESHOLD REDUCTION

### INTRODUCTION

The scaling of lasers to high power often causes a deterioration in the output beam quality. One approach to solving this problem is to use stimulated Brillouin scattering (SBS) phase conjugation techniques [1]. Efficient SBS is routinely achieved in the visible and near-infrared (IR) simply by focusing a laser into a Brillouin cell, but it is more difficult to achieve at longer wavelengths for several reasons. There is an inherent problem with many materials having weak absorption bands in the IR (e.g., as a result of overtones in the C-H vibration mode). Phonon lifetimes increase with the square of the wavelength, so the scattering process takes longer to become established. Another consideration is that experiments to date have used short, high-intensity pulses. Long-pulse or CW lasers will have much lower intensities and require efficient phase conjugation at lower powers.

We carried out a series of experiments by using a 2- $\mu\text{m}$  Ho:YAG laser that gave an output pulse approximately 200-ns long with a repetition rate of 1 Hz. This was more convenient than the previous HF laser source that had a repetition rate of 1 shot per 15 minutes. It was also more relevant than a Nd:YAG laser, which has an output at 1.06  $\mu\text{m}$  and usually produces either a 10-ns long pulse or a 2-ms pulse consisting of a collection of independent spiky relaxation oscillations.

In principle, SBS is characterized by a threshold intensity and a slope efficiency of 100%. In practice however, lower efficiencies are often observed because of other (usually absorption-related) processes. It arises as a result of Brillouin amplification of noise. Threshold depends on the spontaneous noise level and on the Brillouin gain, which depends exponentially on the input intensity and the interaction length. Conjugation occurs because noise conjugate to the input experiences enhanced gain. The key to improving the efficiency of a phase conjugate mirror is reducing the threshold and maintaining the slope efficiency and fidelity.

One approach to threshold reduction is to use long interaction lengths [2, 3]. This can be done by using a light pipe filled with the active liquid. However, this requires suitable materials to provide total internal reflection and a laser with a long coherence length [1]. Alternatively, one can repeatedly refocus a beam through a series of Brillouin cells, with the transit time between foci matching the one-way transit time of the laser cavity [4]. This effectively increases the interaction length without the need for total internal reflection or long coherence lengths.

Alternative approaches get away from the concept of simply increasing the effective Brillouin gain. These techniques are similar to techniques used in photo-refractive phase conjugation [5].

Self-pumped four-wave mixing involves placing an SBS cell in a separate cavity [6]. When an input pump is directed into the cell, Brillouin gain causes the cavity to resonate. The counterpropagating cavity beams can then produce phase conjugation by four-wave mixing. This method can be efficient and has a low threshold, but it requires that the Brillouin cavity be indirectly matched to the laser cavity. Even when this is met, chaotic instabilities that may disrupt its performance can develop [7, 8].

The loop scheme [9] is a more promising scheme. In this, the input beam is passed through a Brillouin cell and brought around. It is then passed through a second time to overlap the beam on the first path. In the overlap region, four-wave mixing can take place and low threshold backscattering is observed.

Finally recent studies have been made of a ring scheme [10] in which the Stokes output of the Brillouin cell is fed back to reseed the input. This has been reported as having an even lower threshold than the loop scheme.

In this report, we consider both the loop and the ring schemes. We first discuss qualitatively the features of the loop scheme and the mechanism responsible for its behavior. Then we review the published literature on the loop scheme, introduce a theory of the loop-SBS interaction, discuss phase conjugation by SBS, and present a steady-state theory,

We then discuss the theory of the ring scheme and compare it with the loop scheme. Finally we describe our experimental setup, which can be used for either the loop or the ring schemes. The discussion includes alignment and the role of various critical parameters. We present energy, intensity, and conjugate fidelity data, and compare these results with theoretical predictions.

## REVIEW OF THE LOOP SCHEME

Figure 1 is a schematic layout of a loop. An input beam  $A_1$  traces its path around the loop and a back-scattered beam emerges as  $A_2$ . In the overlap region, a grating  $u_s$  is driven by interference between  $A_1$  and  $A_4$  and between  $A_2$  and  $A_3$ . Conventional Brillouin amplification may also take place, but the dynamics of the loop can be understood by concentrating on the role of the four-wave mixing grating  $u_s$  alone.

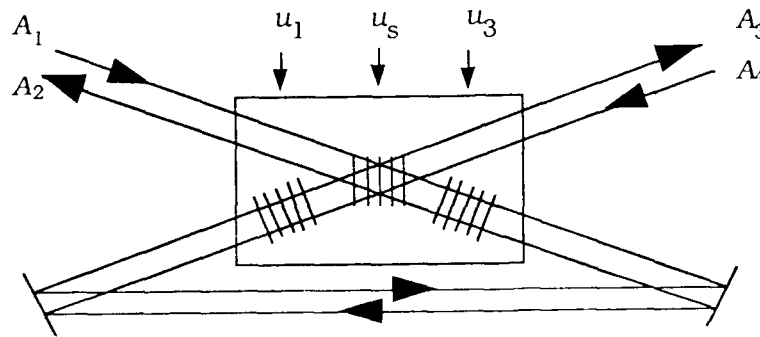


Fig. 1 — Simple loop showing an input beam  $A_1$  tracing its path around the loop and emerging as  $A_3$  after a loop transit time. The input beam is partly scattered by an initially noise-generated acoustic grating  $u_s$  to form  $A_4$  and after a loop transit time  $A_2$ . In the overlap region, the grating  $u_s$  is driven by four-wave mixing interference between  $A_1$  and  $A_4$  and between  $A_2$  and  $A_3$ . Conventional Brillouin amplification may also take place as indicated by gratings  $u_1$  and  $u_3$ .

An incident field  $A_1$  is partially scattered by an initially noise-generated  $u_s$  to form  $A_4$  and partially transmitted. The two fields then pass around the loop in opposite directions and, after a loop transit time, form beams  $A_3$  and  $A_2$ . The interference fringes formed by these two beams amplify the acoustic wave  $u_s$  and scatter more radiation from  $A_3$  into  $A_2$ . If the amplification rate exceeds the natural damping rate, the acoustic wave will grow until pump depletion limits it. Once the acoustic wave is present, the scattering of  $A_1$  at time  $t$  ensures that interference fringes are formed by  $A_2$  and  $A_3$  at a later time over the whole of the interaction volume, and these will reinforce  $u_s$ . Thus there is no need to rely on spontaneous noise to act as a continuous input signal, as is the case with conventional SBS.

The four-wave mixing grating transfers radiation from the pump to the conjugate in two possible ways:  $A_1$  can be scattered on the first transit through the cell and then pass around the loop at the Brillouin-shifted frequency, or it can pass around the loop at the input frequency and then be scattered on the second pass. There is interference between these two paths and the output is a maximum when the phase difference  $\Delta\phi = (k_2 - k_1)L = 2n\pi$ . When the phase difference is not optimized, the threshold increases and the output frequency is pulled from the center of the Brillouin gain curve. This is because an imaginary part of the Brillouin gain (a Brillouin-induced refractive index) is away from line center, and this changes the effective phase difference around the loop.

It is not clear that the loop itself has an intrinsic mechanism that ensures that phase conjugation occurs. Conventional Brillouin amplification produces phase conjugation because the conjugate experiences enhanced gain compared with the nonconjugate and Brillouin amplification may take place in the loop. The Brillouin shift depends on the intersection angle between the signal and the pump, so the degree to which Brillouin amplification occurs will depend on this intersection angle.

The first investigation of a loop scheme was carried out by Odintsov and Rogacheva in 1982 [9]. They used a loop in which the overlapping beams were confined in a 5-cm light guide and reported low-threshold, high-fidelity phase conjugation. Their threshold was reduced by about a factor 10 compared with conventional SBS, and it corrected for an aberrator that increased the input divergence by a factor 10. They also described a simple theory that identified the mechanism as having an "absolute instability" as a result of the role of feedback in the four-wave mixing process.

The implication of an "absolute instability" is that the output grows exponentially in time rather than exponentially in space as in conventional SBS, a "convective instability." Initial noise is required at the start of both types of instabilities. Once an absolute instability has started to develop, however, no further noise is required, and the final output level is independent of the initial noise.

In 1983 Cronin-Golomb et al. [5] discussed various self-pumped schemes for photorefractives, including loops and self-pumped cavities. Subsequently Bel'dyugin and coworkers [11] investigated various loop schemes with, for example, amplifiers inside the loop, and other nonlinearities such as thermal gratings being responsible for the coupling.

Zaskal'ko et al. [12] studied the loop scheme by using a 70-ns Nd:YAG laser pulse with a collimated beam passing through the cell filled with CS<sub>2</sub> or acetone. The threshold was reduced by a factor 2.5 compared with conventional SBS and had a slope efficiency of 75%. At small angles the reflectivity dropped from 70% to 20-30%. Here, the reflectivity developed modulations, a phenomenon that was attributed to forward Brillouin scattering. The beam quality for the loop scheme was found to be better than when normal Brillouin backscattering took place.



Anikeev et al. [13] studied the fidelity of a loop by using a collimated pump beam. They observed a factor 5 reduction in threshold but noted that the backscattered beam had twice the divergence of the input. In general, they found that the spatial structure of the pump was not replicated in the backscattered beam unless some form of discrimination was used to enhance its conjugate properties. This was achieved by inserting an aberrator before the loop, which led to gain enhancement in the conjugate beam. However, the conjugate beam was still imperfectly conjugated. Another method that they suggested was to focus the beam transmitted by the loop into an SBS cell. If the input consisted of a long, low-power input beam with a short high-power leading edge, then the conventional SBS cell would seed the loop for the rest of the input pulse.

The problem of beam quality was investigated by Zozulya et al. [14] who developed a two-dimensional analysis to treat the problem of the crossing beams. They projected the crossing beams onto a coordinate system with the beams propagated orthogonally. The solution obtained was inconsistent with the one-dimensional analysis. They argued that the latter was invalid [15] and made suggestions for improving beam quality. These included physically rotating the beam by  $90^\circ$  between the first and second transit through the loop, and demagnifying the beam so that its diameter is reduced on the second transit compared with the first. They developed this further [16] to quantify the threshold and fidelity as a function of demagnification coefficient.

Eliseev et al. [17] carried out some experiments in which the loop scheme was implemented with beam demagnification. A collimated (1.5-J) beam was passed through the active medium and then reduced in diameter by a factor  $\alpha$  by using a concave mirror before overlapping with the first beam. They measured the fidelity by looking at the reconstruction of an image. The fidelity was found to be highest when  $\alpha \sim 0.6$ - $0.7$  and was noticeably smaller when  $\alpha$  was close to 1 or 0.1, matching predictions. They observed a maximum reflectivity of 30-40% and a slope efficiency of less than 100%, contrary to the simple one-dimensional theory.

Anikeev et al. [18] examined another factor affecting beam quality. For a given loop length, there is a phase difference between light that travels the path at the input wavelength and the conjugate beam returning along the same path. The threshold for the loop is a minimum when the phase shift is an integer multiple of  $2\pi$ . A nonconjugate beam will travel around a different path and hence have a different phase difference. If the loop is operated so that the phase difference is close to resonance (i.e., the threshold for the conjugate is close to maximum), a nonconjugate path that has a lower threshold may exist for the backscattered beam. Experimentally this was detected by measuring a modulation that results from beating between the conjugate and this nonconjugate component.

Zhanuzakov et al. [19] returned to the one-dimensional analysis to calculate the steady-state reflectivity of a loop, noting the difficulties of the more encompassing two-dimensional analysis. They neglected Brillouin amplification, assuming a large intersection angle between the overlapping beams. Among their conclusions, they noted that the maximum possible reflectivity depended on the phase difference  $\Delta\phi$  between the signal and Stokes beams in their transit around the loop, with the maximum reflectivity depending on  $\cos^2 \Delta\phi$ . They predicted highly nonlinear reflection coefficients with many different frequency components, particularly in the case of long loop lengths. They later investigated [20] whether the steady-state backscattering in a loop was stable, and concluded that instabilities will develop when the steady-state threshold is exceeded by a factor 3 to 6.

In some circumstances, modulation of the backscattered and transmitted beams was observed. This was suggested as being due to forward Brillouin scattering. Andreev et al. [21] modeled this problem and

noted that this forward SBS may occur. However, depending on the phase shift around the cavity, this need not greatly reduce the loop efficiency.

The Brillouin interaction is driven by the moving interference fringes in the active medium. Andreev et al. [22] calculated the effect of the stationary interference fringes and concluded that they increased the threshold intensity, reduced the fidelity, and hindered the establishment of a steady state regime.

Nikolaev and Odintsov [23] studied the performance of a loop in which the overlap region was formed by two beams that were nearly counter-propagating rather than nearly copropagating as in the usual geometry. They found that this reduced the threshold by nearly a factor 2 compared with the usual loop. They also varied the loop length and noted that the threshold varied by 30% when the loop length was changed by 3 cm, matching the theoretical prediction that the threshold depends on the phase difference  $\Delta\phi$ .

Eliseev and Tikhonchuk [24] analyzed the performance of a ring in terms of eigenmodes and used this to assess phase conjugate beam quality for various degrees of compression. A detailed review of much of the recent Russian analytical work, particularly the two-dimensional analysis, has recently been published by Tikhonchuk and Zozulya [25].

## REVIEW OF THE RING SBS SCHEME

The ring scheme has been investigated by fewer workers. Wong and Damzen [10] described some studies based on both the loop and ring geometries. The ring geometry, previously proposed by Shakir [26] provides an arrangement whereby the transmitted beam is fed back to overlap the initial beam in the Brillouin medium. They carried out a steady-state analysis to show that a ring would have high efficiency and a low threshold. They also modeled the transient behavior and found good agreement between theory and experiment for the ring. The threshold was reduced by a factor 1.4, and the reflectivity increased much more rapidly than with conventional SBS. When they went to the loop, they had much poorer agreement between their model and experiment.

The approach we have taken has been determined partly by the components available and partly by the desire to investigate a compact, low-threshold system for a multiple transverse-mode laser with an overall coherence length of  $\sim 50$  cm. This latter requirement restricts us to using focused beams, with consecutive foci separated by a transit time matching an integral multiple of the transit time of the laser cavity to ensure mutual coherence. We included a second intermediate focus in the loop for convenience of alignment, and the analysis includes this auxiliary Brillouin amplifier. We also reformulated the one-dimensional analysis to deal with the loop problem in a way to make it more directly comparable with the experiments, particularly including the Brillouin amplifier and the effect of partial overlap.

## THEORY OF THE LOOP-SBS INTERACTION

We analyze the behavior of a loop-SBS mirror, paying particular attention to parameters that can be influenced by experiment. We experimentally investigate the case of partially overlapping focused beams that cross at a small angle and use a uniform one-dimensional plane wave approximation. Factors to account for the partial overlap and the effect of focusing are introduced.

The scheme is implemented by first focusing a beam through a Brillouin cell, collecting the transmitted beam. This is then recollimated and directed back to the input side of the cell. It is again

refocused through the cell so that the second focus overlaps the first. Brillouin four-wave mixing takes place where the beams overlap; additionally, Brillouin amplification may take place outside the overlap region. In our experiment we have refocused the beam through the active medium on its path back to the front of the cell. This provides an extra zone where Brillouin amplification may take place.

We use the notation of Ref. 27 and assume plane waves overlapping (Fig. 2). We assume that the input beam enters the cell at  $r = 0$  as beam 1, and is then directed through the cell a second time as beam 3. We consider the behavior of a Brillouin-shifted beam 4, which propagates from  $r = L$  counter to beam 3 and is then passed around to form beam 2, which propagates counter to beam 1:

$$\begin{aligned} \mathcal{E}_j(\underline{r}, t) &= \frac{1}{2} E_j(\underline{r}, t) \exp\{i(\omega_j t - \underline{k}_j \cdot \underline{r})\} + c.c.; \quad j = 1, 2, 3, 4; \\ \omega_1 &= \omega_3; \quad \omega_2 = \omega_4; \quad \omega_2 = \omega_1 - \Delta\omega; \\ \underline{k}_2 &= -\underline{k}_1; \quad \underline{k}_4 = -\underline{k}_3; \quad \Delta \underline{k} = -\underline{k}_1 - \underline{k}_2 + \underline{k}_3 + \underline{k}_4 = 0. \end{aligned} \quad (1)$$

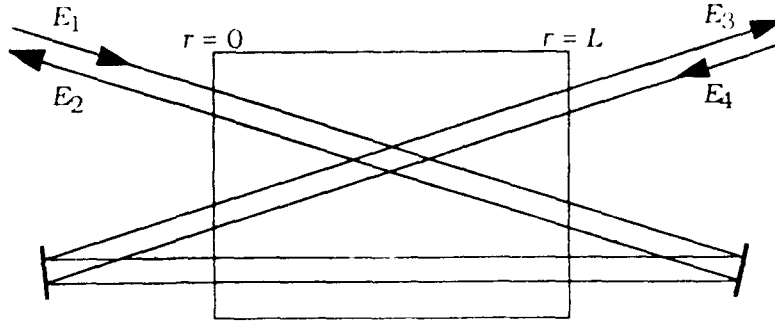


Fig. 2 -- Plane waves overlapping in a Brillouin active medium

The overlapping beams produce interference fringes:

$$\begin{aligned} (\sum_j \mathcal{E}_j)^2 &= \dots + \frac{1}{2} E_1 E_2^* \exp\{i(\Delta\omega t - 2\underline{k}_1 \cdot \underline{r})\} + \frac{1}{2} (E_1 E_4^* + E_2^* E_3) \exp\{i(\Delta\omega t - \underline{k}_s \cdot \underline{r})\} \\ &\quad + \frac{1}{2} E_3 E_4^* \exp\{i(\Delta\omega t - 2\underline{k}_3 \cdot \underline{r})\} + c.c. \end{aligned} \quad (2)$$

In the above  $\underline{k}_s$  is the wave vector of the interference pattern formed by  $\underline{k}_1$  and  $\underline{k}_4$ , and is defined by:

$$\underline{k}_s = \underline{k}_1 - \underline{k}_4; \quad k_s = 2k_1 \cos \theta, \quad (3)$$

where  $2\theta$  is the angle between  $\underline{k}_1$  and  $\underline{k}_3$ .

The interference fringes in turn drive acoustic waves:

$$\begin{aligned} \mathcal{U}_1 &= \frac{1}{2} u_1 \exp\{i(\Delta\omega t - 2k_1 r)\} + c.c. \\ \mathcal{U}_s &= \frac{1}{2} u_s \exp\{i(\Delta\omega t - k_s r)\} + c.c. \\ \mathcal{U}_3 &= \frac{1}{2} u_3 \exp\{i(\Delta\omega t - 2k_3 r)\} + c.c. \end{aligned} \quad (4)$$

The acoustic waves have resonant frequencies  $\omega_{s1}$  determined by the speed of sound in the medium  $v_s$  and the wave vectors of the interference patterns that drive them:

$$\omega_{s1} = 2k_1 v_s = 2k_3 v_s = \omega_{s3} ; \quad \omega_{s5} = 2k_1 v_s \cos \theta . \quad (5)$$

The interference terms produce an electrostrictive force that drives the acoustic waves:

$$\begin{aligned} (1 + ix_1)u_1 + \frac{1}{\delta\omega_0} \frac{\partial u_1}{\partial t} &= -\beta E_1 E_2^* , \\ (1 + ix_s)u_s + \frac{1}{\delta\omega_0} \frac{\partial u_s}{\partial t} &= -\beta(E_1 E_4^* + E_2^* E_3) , \\ (1 + ix_1)u_3 + \frac{1}{\delta\omega_0} \frac{\partial u_3}{\partial t} &= -\beta E_3 E_4^* . \end{aligned} \quad (6)$$

The first and third equations correspond to conventional Brillouin amplification; the second corresponds to Brillouin four-wave mixing.  $\beta$  is a coupling constant, and the parameter  $\delta\omega_0$  is the Brillouin linewidth (HWHM), given by:

$$\delta\omega_0 = \frac{1}{2} \alpha_s v_s = \frac{1}{2\tau_B} , \quad (7)$$

where  $\tau_B$  is the decay time of the acoustic intensity. The decay time is weakly wavelength dependent, and hence angle dependent. However for small angles this can be neglected:

$$\delta\omega_0(\theta) \propto 1/\lambda^2 \propto \cos^2 \theta .$$

In Eq. (6) we also introduced detuning parameters  $x_1$  and  $x_s$ , which give the ratio of the detuning from the center of the Brillouin gain curve to the Brillouin linewidth:

$$x_1 = (\Delta\omega - \omega_{s1}) / \delta\omega_0 ; \quad x_s = (\Delta\omega - \omega_{s5}) / \delta\omega_0 = x_1 + (1 - \cos \theta) \omega_{s1} / \delta\omega_0 . \quad (8)$$

When  $x = 0$ , we are at the center of the Brillouin gain curve. Inspection by using the values in Table 1 indicates that if  $q$  is more than a few mrad, the detuning between  $\omega_{s5}$  and  $\omega_{s1}$  may be comparable to the Brillouin linewidth.

The acoustic waves scatter the four electric fields:

$$\begin{aligned} \frac{\partial E_1}{\partial r} &= \frac{g}{2\beta} (h_1 E_2 u_1 + h_s E_4 u_s) \\ \frac{\partial E_2}{\partial r} &= \frac{g}{2\beta} (h_1 E_1 u_1^* + h_s E_3 u_s^*) \\ \frac{\partial E_3}{\partial r} &= \frac{g}{2\beta} (h_s E_2 u_s + h_3 E_4 u_3) \\ \frac{\partial E_4}{\partial r} &= \frac{g}{2\beta} (h_s E_1 u_s^* + h_3 E_3 u_3^*) . \end{aligned} \quad (9)$$

Table 1 - Sample Values of Brillouin Parameters for  $\lambda = 2.1 \mu\text{m}$ 

Medium	CS <sub>2</sub> [a]	SnCl <sub>4</sub> [b]	Xe (39 atm) [c]
Gain coefficient $g$ (cm/GW)	130, 65 [d]	11.2	44
Brillouin shift $\nu_s$ (GHz)	1.69	1.11	0.16
$\omega_s$ (rad/s)	$1.06 \times 10^{10}$	$6.97 \times 10^9$	$1 \times 10^9$
Phonon lifetime $\tau_B$ (ns)	20	7	132
Linewidth $\delta\omega_0$ (rad/s)	$2.5 \times 10^7$	$7.2 \times 10^7$	$3.8 \times 10^6$
Mode spacing $c/1.8 \text{ m}$ (Hz)	$1.67 \times 10^8$	$1.67 \times 10^8$	$1.67 \times 10^8$
Detuning: $x_1 = 0$			
$\theta = 5 \text{ mrad}$ : $x_s$	$5.3 \times 10^{-3}$	$1.2 \times 10^{-3}$	$3.3 \times 10^{-3}$
$\theta = 50 \text{ mrad}$ : $x_s$	$5.3 \times 10^{-1}$	$1.2 \times 10^{-1}$	$3.3 \times 10^{-1}$

- [a] D. Pohl and W. Kaiser, "Time-resolved Investigations of Stimulated Brillouin Scattering in Transparent and Absorbing Media: Determination of Phonon Lifetimes," *Phys. Rev. B* **1**, 31 (1970).
- [b] S. T. Amimoto, R. W. F. Gross, L. Garman-DuVall, T. W. Good, and J. D. Piranian, "Stimulated-Brillouin-scattering Properties of SnCl<sub>4</sub>," *Opt. Lett.* **16**, 1382 (1991).
- [c] V. I. Kovalev, V. I. Popovichev, V. V. Ragul'skii, and F. S. Faizullov, "Gain and Linewidth in Stimulated Brillouin Scattering in Gases," *Sov. J. Quantum Electron.* **2**, 69 (1972).
- [d] A. I. Erokhin, V. I. Kovalev, F. S. Faizullov, "Determination of the parameters of a Non-linear Response of Liquids in an Acoustic Resonance Region by the Method of Nondegenerate Four-wave Interaction," *Sov. J. Quantum Electron.* **16**, 872 (1986); K. D. Ridley, A. M. Scott, and D. C. Jones, "Frequency Detuning in Brillouin-Induced Four-Wave Mixing," *Int. J. Non-linear Opt. Phys.* **1**, 563 (1992).

In Eq. (9)  $g$  is the Brillouin gain coefficient, and  $h_1$ ,  $h_2$ , and  $h_s$  are empirical "enhancement factors" that are discussed in the next section. For now we note that these factors can be unity in the case of perfect plane waves.

Equations (6) and (9) together form a set of equations that describe the transient and steady-state behavior of the loop geometry. They assume the slowly varying wave approximation and neglect spontaneous noise. The equations also require appropriate boundary conditions to define the problem fully.

## PHASE CONJUGATION BY STIMULATED BRILLOUIN SCATTERING

Before tackling the problem of the loop SBS scheme, we review the features of phase conjugation by SBS. We can study the steady-state behavior of a Brillouin amplifier by using the above equations with  $E_3 = E_4 = 0$ , and  $u_s = u_2 = 0$ .

SBS is a result of a convective instability in which the output is the result of high gain amplification of spontaneous noise, which is always present at a level of about  $\exp(-25)$  of the incident pump beam. Over long time scales variations in the noise occur that are detectable in the scattered beam [28].

Two mechanisms contribute to producing an apparently phase conjugate SBS beam. The first mechanism is gain enhancement. This arises when the speckle structure of the aberrated beam produces large spatial variations in intensity in the focal volume of the focused pump beam. The Brillouin gain is

average net gain coefficient. The enhancement factor depends on the precise speckle structure of the pump beam and is usually assumed to be 2 [1]. There will always be some component of noise that is conjugate to the input, and this will experience the enhanced gain.

The second mechanism for producing apparent phase conjugation is the fact that the source of the SBS beam is the focal volume of the pump beam. This is more precisely a mechanism for retroreflection; the SBS is not truly conjugate. In the near field it may have noticeably poor fidelity, but in the far field (which is the image of the focal spot in the SBS cell) the beam will often match the structure of the input beam. This latter mechanism will give the SBS beam an appearance of being phase conjugate when the beam has little speckle structure and gain enhancement does not take place, as in the case of a near diffraction limited input beam [1].

### Steady State Brillouin Amplifier

If we take Eqs. (6) and (9) and use  $E_3 = E_4 = 0$ , and  $u_s = u_2 = 0$ , we get:

$$\frac{\partial I_1}{\partial r} = \frac{h_1 g_B I_1 I_2}{(1+x^2)} = \frac{\partial I_2}{\partial r}, \quad (10)$$

where

$$\frac{1}{2} \epsilon_0 |E_i|^2 = I_i / c; \quad g_B I_i = g |E_i|^2. \quad (11)$$

If the input of the Brillouin amplifier is a specific signal, then  $x$  will be determined by the frequency of the signal. If the 'signal' is spontaneous noise, then it will have a broad spectrum and the resonant component will be amplified and  $x$  can be taken to be zero.

The reason for introducing  $h_1$  is now apparent.  $h_1$  is the enhancement factor discussed above. It equals 1 when  $E_1$  and  $E_2$  are plane waves, and we assume a value of 2 when calculating the role of gain enhancement in the conjugate beam.

Equations (10) have as a solution

$$\frac{I_2(0)}{I_2(L)} \frac{I_1(L)}{I_1(0)} = \exp\{h_1 g_B (I_1 - I_2)L\}; \quad (12a)$$

$$I_1(L) - I_2(L) = I_1(0) - I_2(0). \quad (12b)$$

In the absence of pump depletion, this reduces to

$$I_2(0) = I_2(L) \exp\{g_B I_1 L\}. \quad (13)$$

Equation (12) emphasizes that if there is no input signal [ $I_2(L) = 0$ ], the output SBS intensity  $I_2(0)$  will also be zero. In the absence of an applied signal, spontaneous noise [which is present at an intensity exp (-25) less than the pump beam] will act as the signal.

We can use Eq. (12) to calculate the scattering efficiency. First we calculate the transmission of the pump beam. If we write  $I_2(L) = qI_1(L)$ , where  $q$  is a spontaneous scattering coefficient, we obtain

$$I_1(0) = \frac{I_1(L)}{1 - q \exp\{h_1 g_B I_1(L)L\}}. \quad (14)$$

As  $h_1 g_B I_1(L)L \rightarrow -\log(q)$ ,  $I_1(0) \rightarrow \infty$ .

Equation (14) plus Eq. (12b) shows that the SBS output is characterized by a threshold  $h_1 g_B I_1(0)L = -\log(q) \approx 25$  and a slope efficiency of 100%. This also indicates that the threshold for phase conjugate SBS will be approximately a factor 2 less than the threshold for nonconjugate SBS (Fig. 3).

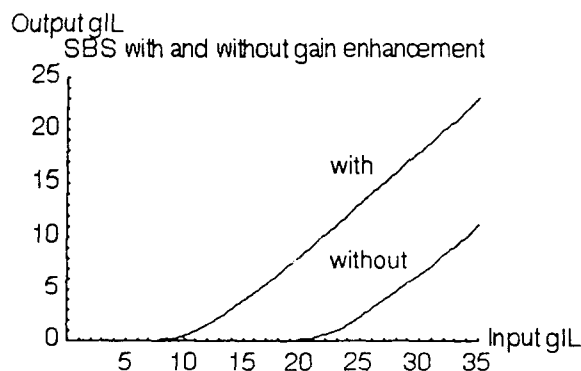


Fig. 3 — Output  $gIL$  vs input  $gIL$  with and without gain enhancement

We return to the equations above, which describe a Brillouin amplifier. The expression for  $I_1(r)$  makes it possible to integrate the equation for  $dE/dr$  to determine the Brillouin-induced phase shift.

We conclude this discussion by mentioning the transient behavior. In the transient regime, the Stokes intensity is given by:

$$I_2(t) \sim \exp(-\delta\omega_0 t + \sqrt{h_1 g_B I_1 L \delta\omega_0 t}), \quad (15)$$

which does not simply grow exponentially with time.

In summary, phase conjugation by SBS is characterized by nonexponential transient behavior, a threshold dependent on the spontaneous noise, a 100% slope efficiency in principle, and conjugation occurring because of enhancement in the effective gain coefficient due to speckle intensity fluctuations.

### Overlapping Gaussian Beams

This section describes features associated with focusing of the beams. We first develop a model for the loop geometry by considering two focused Gaussian beams that intersect at their waists. Figure 4 shows the geometry to be characterized by an intensity overlap region with length  $L_{eff}$  where four-wave mixing can take place, and interaction regions with length  $L_t$  where Brillouin amplification can take place.

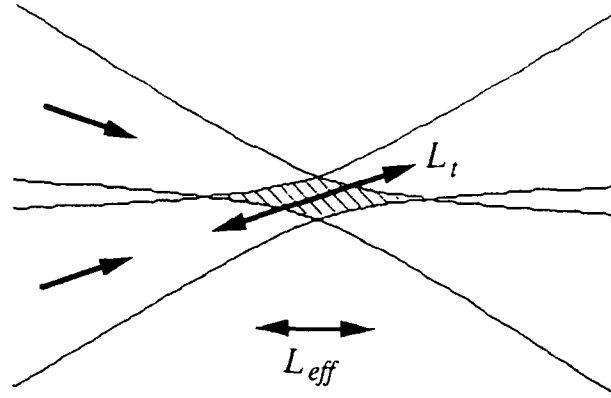


Fig. 4 — Two Gaussian beams overlapping at their waists.  $L_{eff}$  indicates the length of the intensity overlap region where four-wave mixing can occur, and  $L_t$  indicates the length of the Brillouin amplification region.

We consider beams intersecting at angle  $2\theta$  in the  $y$ - $z$  plane. The two beams have axes  $y = \pm z \sin \theta$  and intensities given by Ref. 29:

$$I_1(r) = \frac{2P_1}{\pi\omega^2} \exp\left\{-\frac{2x^2}{\omega^2} - \frac{2(y+z \sin \theta)^2}{\omega^2}\right\}$$

$$I_2(r) = \frac{2P_2}{\pi\omega^2} \exp\left\{-\frac{2x^2}{\omega^2} - \frac{2(y-z \sin \theta)^2}{\omega^2}\right\},$$
(16)

where the radius of the beam  $\omega$  is given by

$$\omega^2 = \omega_0^2 \left(1 + \frac{z^2}{z_0^2}\right),$$
(17)

$\omega_0$  is the waist located at  $z = 0$ ,  $z_0$  is the value of  $z$  where the beam expands by  $\sqrt{2}$ , and  $P_1$  and  $P_2$  are the powers of beams 1 and 2 respectively.

The growth rate is given by Eq. (10)

$$\frac{\partial I_1}{\partial r} = h_1 g_B I_1 I_2.$$
(10)

This can be integrated over the  $x$ - $y$  plane to give:

$$\frac{dP_2}{dz} = \frac{h_1 g_B P_1 P_2}{\pi \omega_0^2} J(z); \quad J(z) = \frac{\exp\left\{\frac{-4z^2 \sin^2 \theta}{\omega_0^2 [1 + z^2 / z_0^2]}\right\}}{(1 + z^2 / z_0^2)}.$$
(18)



Integrating over  $z = \pm\infty$  gives

$$\int_{-\infty}^{\infty} \frac{dP_2}{P_2} = \log \frac{P_2(0)}{P_2(L)} = \frac{h_1 g_B P_1 z_0}{\omega_0^2} f_0, \quad (19)$$

where

$$f_0 = \frac{1}{\pi} \int_{-\infty}^{\infty} \frac{\exp\left\{\frac{-A^2 u^2}{1+u^2}\right\}}{[1+u^2]} du; \quad A = \frac{2z_0 \sin \theta}{\omega_0} \approx \frac{2\theta_{sep}}{\theta_{div}} \quad (20)$$

$$\theta_{sep} = 2\theta; \quad \theta_{div} = 2\omega_0 / z_0,$$

as  $\theta \rightarrow 0 \Rightarrow f_0 \rightarrow 1$ .

The parameter  $f_0$  is the overlap parameter and describes the degree of overlap of the two foci. When  $f_0 = 1$ , the two beams fully overlap and we can define the mean pump intensity and interaction length as:

$$I_1 = P_1 / \pi \omega_0^2; \quad L_t = \pi z_0. \quad (21)$$

It is straightforward to show that when the angle of separation between the two beams  $\theta_{sep} = 2\theta$  becomes comparable with the divergence of the focused beam  $\theta_{div} = 2\omega_0/z_0$ , then  $f_0$  and the effective interaction length  $L_{eff}$  for the overlapping beams become:

$$f_0 \approx \frac{\theta_{div}}{2\sqrt{\pi}\theta_{sep}}; \quad L_{eff} = L_t f_0. \quad (22)$$

In Fig. 5 we plot the overlap parameter obtained from Eq. (20) and compare it with the approximation in Eq. (22).

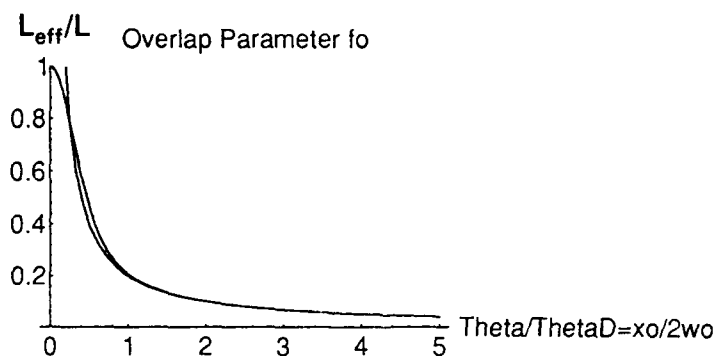


Fig. 5 — Comparison of overlap parameter as function of  $\theta_{sep}/\theta_{div}$  calculated by using Eqs. (20) and (22)

Experimentally we do not wish to let the beams obstruct each other in the far field. This means that, in practice, we tend to operate with  $\theta_{\text{sep}}/\theta_{\text{div}} \geq 1$ , i. e., with  $f_0 \leq 0.2$ . Note also that the overlap parameter reaches 0.8 when  $\theta_{\text{sep}}/\theta_{\text{div}} < 0.4$ . This aspect can be used to explain why SBS formed from a Gaussian beam can produce an apparently conjugate beam even though the mechanism of gain enhancement is not occurring.

In the following sections we use the one-dimensional analysis with interaction lengths and intensities determined by Eq. (21) and (22).

### Theory of the Loop-SBS Geometry

When two focused beams cross, there will be an overlap region where Brillouin amplification and four-wave mixing may take place; outside this region, Brillouin amplification alone may occur. Our particular experiment has a second intermediate focus where Brillouin amplification is possible. We model this by considering a system of two coupled nonlinear regions (Fig. 6).

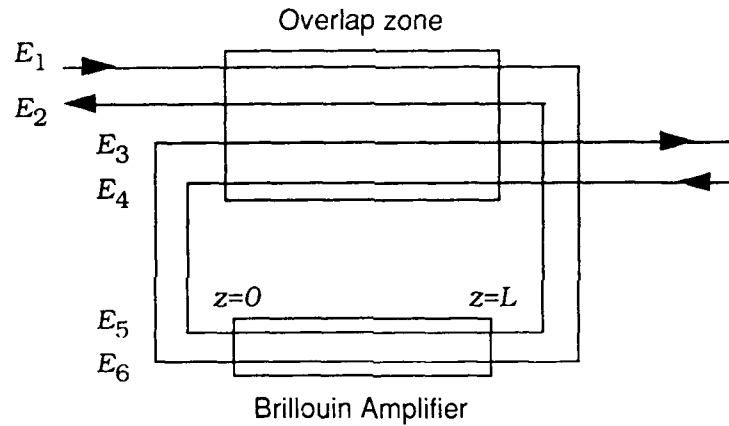


Fig. 6 — Model used for separately considering the four-wave mixing and Brillouin amplification regions

We lump together all the regions where Brillouin amplification can take place but four-wave mixing cannot. This is done to prevent an excess of minor variables from obscuring the physics of the interaction. The equations for  $E_5$  and  $E_6$  can be obtained directly from above with a suitable renaming of variables.

We take the interaction length for the overlap zone to be  $L = f_0 L_t$  and for the amplifier to be  $L_A = (2 - f_0) L_t$ . The boundary conditions become:

$$\begin{aligned}
 E_1(r=0, t) &= E_{in}; \\
 E_6(r_A = L_A, t) &= \gamma_1 E_1(r = L, t - t_1); \\
 E_3(r=0, t) &= \gamma_2 E_6(r_A = 0, t - t_2) \exp i \phi_A; \\
 E_4(r = L, t) &= 0; \\
 E_5(r=0, t) &= \gamma_2 E_4(r = 0, t - t_2) \exp i \phi_S; \\
 E_2(r = L, t) &= \gamma_1 E_5(r_A = L_A, t - t_1).
 \end{aligned}
 \tag{23}$$

In the above,  $\gamma_1$  and  $\gamma_2$  are the amplitude reflection coefficients for mirrors on either side of the loop,  $t_1$  and  $t_2$  are the relevant transit times ( $t_1 + t_2 = t_c$  is the round loop transit time), and  $\phi_A$  and  $\phi_S$  are the phase shifts around the loop for frequencies  $\omega_1$  and  $\omega_2$  respectively.

The phase shift for the Stokes beam is given by

$$\phi_S = k_S L_{loop} = \omega_S L_{loop} / c = \phi_A - \omega_S L_{loop} / c - x_1 \delta \omega_0 L_{loop} / c. \quad (23a)$$

### Transient Behavior of the SBS Loop

We calculate the transient behavior of the SBS-loop system by assuming undepleted pump beams, i.e.,  $E_1, E_3, E_6$  are all constant when  $t > 0$ , and zero when  $t < 0$ . This gives  $E_6 = \gamma_1 E_1$ ;  $E_3 = \gamma_1 \gamma_2 E_1$ .

We apply a Laplace transform to Eq. (6) and obtain

$$\begin{aligned} [\delta \omega_0 (1 + ix_1) + s] \bar{u}_1 &= -\beta \delta \omega_0 E_1 \bar{E}_2^* \\ [\delta \omega_0 (1 + ix_s) + s] \bar{u}_s &= -\beta \delta \omega_0 (E_1 \bar{E}_4^* + \bar{E}_2^* E_3) \\ [\delta \omega_0 (1 + ix_1) + s] \bar{u}_3 &= -\beta \delta \omega_0 E_3 \bar{E}_4^* \\ [\delta \omega_0 (1 + ix_1) + s] \bar{u}_A &= +\beta \delta \omega_0 \bar{E}_5 E_6^* \end{aligned} \quad (24)$$

where  $s$  is the transform variable. We assume  $x_1 = x_s$ , which is valid for small angles.

The equation for the Brillouin amplifier section can be simplified. The equation for  $\bar{E}_5$  is taken as

$$\frac{\partial \bar{E}_5}{\partial r} = \frac{g}{2\beta} h_1 E_6 \bar{u}_A. \quad (25)$$

When combined with Eq. (24), this has the solution

$$\bar{E}_5(L_A) = \bar{E}_5(0) \exp \left\{ \frac{h_1 g \delta \omega_0 \gamma_1^2 |E_1|^2 L_A}{2[\delta \omega_0 (1 + ix_1) + s]} \right\}. \quad (26)$$

The equations for  $\bar{E}_2^*$  and  $\bar{E}_4^*$  become

$$\begin{aligned} \frac{\partial \bar{E}_2^*}{\partial r} &= -\{h_1 |E_1|^2 \bar{E}_2^* + |E_3|^2 \bar{E}_2^* + E_1 E_3^* \bar{E}_4^*\} S \\ \frac{\partial \bar{E}_4^*}{\partial r} &= -\{h_1 |E_3|^2 \bar{E}_4^* + |E_1|^2 \bar{E}_4^* + E_1^* E_3 \bar{E}_2^*\} S \\ S &= \frac{g \delta \omega_0}{2[\delta \omega_0 (1 + ix_s) + s]}. \end{aligned} \quad (27)$$

In the above we have taken  $h_s$  to be 1 since there are no solid grounds for choosing otherwise. We have also neglected the difference between  $x_s$  and  $x_1$ . If necessary, the effect can be incorporated into  $h_1$ , giving it a complex value.

The coupled equations in Eq. (27) can be decoupled to form two second-order equations

$$\begin{aligned} \frac{\partial^2 \bar{E}_2^*}{\partial r^2} + S(1+h_1)(|\bar{E}_1|^2 + |\bar{E}_3|^2) \frac{\partial \bar{E}_2^*}{\partial r} + S^2(h_1^2|\bar{E}_1|^2|\bar{E}_3|^2 + h_1(|\bar{E}_1|^4 + |\bar{E}_3|^4))\bar{E}_2^* &= 0 \\ \frac{\partial^2 \bar{E}_4^*}{\partial r^2} + S(1+h_1)(|\bar{E}_1|^2 + |\bar{E}_3|^2) \frac{\partial \bar{E}_4^*}{\partial r} + S^2(h_1^2|\bar{E}_1|^2|\bar{E}_3|^2 + h_1(|\bar{E}_1|^4 + |\bar{E}_3|^4))\bar{E}_4^* &= 0. \end{aligned} \quad (28)$$

These equations have solutions

$$\begin{aligned} \bar{E}_2^* &= \bar{E}_{2a}^* \exp(\lambda_a r) + \bar{E}_{2b}^* \exp(\lambda_b r); \\ \bar{E}_4^* &= \bar{E}_{4a}^* \exp(\lambda_a r) + \bar{E}_{4b}^* \exp(\lambda_b r); \\ \lambda_{a,b} &= -\frac{S}{2}(1+h_1)(|\bar{E}_1|^2 + |\bar{E}_3|^2) \pm \frac{w}{2}|\bar{E}_1|^2 S; \\ w^2 &= (1+h_1)^2(|\bar{E}_1|^2 + |\bar{E}_3|^2)^2 - 4h_1(|\bar{E}_1|^4 + |\bar{E}_3|^4 + h_1|\bar{E}_1|^2|\bar{E}_3|^2). \end{aligned} \quad (29)$$

The variable  $w$  can be written as

$$\begin{aligned} w &= w_1|\bar{E}_1|^2; \quad T = \gamma_1^2 \gamma_2^2; \\ w_1^2 &= (1+T)^2 - h_1(2-h_1)(1-T)^2, \end{aligned} \quad (30)$$

where  $T$  is the transmission coefficient around the loop.

This simplifies in three cases of interest:  $h_1 = 0$ , 1, and 2:

$$h_1 = 0 \text{ or } 2 \Rightarrow w_1 = 1+T; \quad h_1 = 1 \Rightarrow w_1 = 2\sqrt{T}. \quad (31)$$

The three cases correspond to the following:  $h_1 = 0$  corresponds to a large angle between the two beams so that the four-wave-mixing resonant frequency  $\omega_s$  is greatly detuned from the normal Brillouin resonance frequency. In that case, Brillouin amplification cannot contribute to the interaction.  $h_1 = 1$  corresponds to the case of small angles with the two resonant frequencies matching but no gain enhancement for the conjugate beam.  $h_1 = 2$  corresponds to resonance, but with phase conjugate gain enhancement occurring in the Brillouin amplification process.

We consider the boundary value of  $\bar{E}_4^* = 0$  at  $r = L$ . This implies

$$\bar{E}_{4a}^* = -\bar{E}_{4b}^* \exp\{-Sw_1|\bar{E}_1|^2 L\}. \quad (32)$$

When this is substituted in the coupled Eqs. (27), the result is

$$\bar{E}_{2a,b}^* = \frac{E_1}{2E_3} \bar{E}_{4a,b}^* [(h_1 - 1)(1 - T) \mp w_1]. \quad (33)$$

We now return to the boundary conditions [Eqs. (23)] for the loop. When we apply the Laplace transform we obtain

$$\begin{aligned} \bar{E}_2^*(r = L, s) &= \gamma_1 \bar{E}_5(r_A = L_A, s) \exp(-st_1) \\ \bar{E}_5^*(r_A = 0, s) &= \gamma_2 \bar{E}_4(r = 0, s) \exp(i\phi_s - st_2). \end{aligned} \quad (34)$$

These can be combined with Eq. (26) to link  $\bar{E}_2^*$  to  $\bar{E}_4^*$ . Combining this with Eq. (33) we can eliminate the constants  $\bar{E}_{2a,b}^*$ ,  $\bar{E}_{4a,b}^*$ . This yields

$$\begin{aligned} \log\left\{\frac{w_1}{T[1 - \exp(-Sw_1|E_1|^2 L)]}\right\} &= -st_c - i(\phi_s - \phi_A) \\ &+ \frac{1}{2}S[2\gamma_1^2 h_1 L_A / L + w_1 + (1 + h_1)(1 + T)]|E_1|^2 L. \end{aligned} \quad (35)$$

Since  $S$  is defined by Eq. (27), there are only two variables,  $s$  and  $x$ , which are free in Eq. (35). We require equality in the real and imaginary parts, and this leads to fixed values for  $s$  and  $x$ .

Applying the inverse transform, we find that the solution is

$$E_2^*(r = 0) = E_0 \exp(st), \quad (36)$$

where  $E_0$  is some initial field, e.g., resulting from spontaneous scattering. The real part of  $s$  will be a growth or decay rate, while  $x$  will be such that the imaginary part of  $s$  is zero (to maintain a consistent definition of  $\omega_2$ ).

The phase shift  $\Delta\phi = \phi_A - \phi_s$  is given by

$$\Delta\phi = \phi_A - \phi_s = -n \Delta\omega L_c / c = -\omega_B L_c / c - x \delta\omega_0 L_c / c, \quad (37)$$

where  $L_c$  is the path length around the loop. This relation means that  $\Delta\phi$  changes by  $2\pi$  over a change in the path length of a few cm.

The growth or decay rate of the intensity  $I_2$  is given by  $2s$ , and we multiply this by the phonon lifetime to get a dimensionless growth rate  $p$ :

$$p = 2s\tau_B = s / \delta\omega_0. \quad (38)$$

We also define a dimensionless intensity parameter  $M_1$ :

$$M_1 = g|E_1|^2 L_t = g|E_1|^2 L / f_0. \quad (39)$$

In Eq. (39),  $L_t$  is the effective length of the focal volume while  $L$  is the length of the overlap region. The definition of  $M_1$  makes it independent of overlap parameter and makes it possible to directly compare the predictions of the theory with the single-focus SBS threshold where  $M_{thresh} \sim 25$ .

In the following discussion we have investigated the behavior of  $p$  and the influence of various parameters. Unless otherwise stated we have used values:

$$\begin{aligned} L_A / L &= (2 - f_0) / f_0; \\ \gamma_1^2 &= 0.8; \quad \gamma_2^2 = 0.8; \quad \Delta\phi = 0; \\ t_c &= 6 \text{ ns}; \quad \tau_B = 20 \text{ ns}; \quad t_{pulse} = 210 \text{ ns}. \end{aligned} \quad (40)$$

Figure 7 is a plot of growth rate  $p$  vs intensity  $M_1$  for three different values of cavity transit time  $t_c$ . At low intensity  $p$  tends to  $-1$ , corresponding to the normal decay of any Stokes radiation in the loop. Above some instability threshold,  $p$  becomes positive and any Stokes radiation will grow exponentially in time and continue to do so until effects such as pump depletion limit it. The figure also illustrates that the instability threshold is independent of the cavity round-trip time; above threshold, the presence of a long cavity causes the build up rate to be reduced.

Growth Rate ( $1/t_B$ )

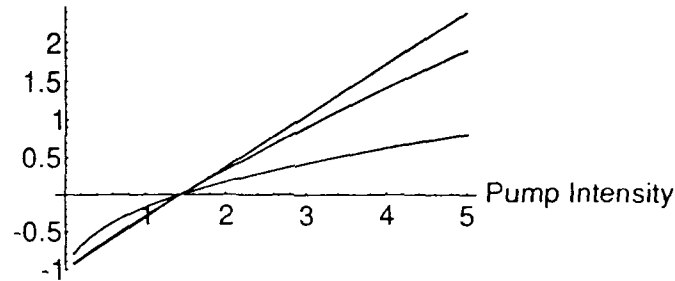


Fig. 7 — Growth rate  $p$  vs pump intensity  $M_1$  for three different values of cavity transit time  $t_c$ . Curves correspond to  $t_c = 0.6 \text{ ns}$ ,  $6 \text{ ns}$ ,  $60 \text{ ns}$  respectively for top, middle, and bottom curves on right-hand side.

This "absolute instability" requires some initial noise to be present so that radiation in the loop can build up. But unlike the "convective instability" of conventional SBS, the noise is no longer needed once the process is under way. The instability threshold itself is not dependent on the noise intensity. The graph shows that the instability threshold is almost a factor 20 less than the SBS threshold, an observation made by several authors [9, 10].

The time constant can be very large near threshold, and the effect of the instability will not be observed in practice unless spontaneous noise has built up to become comparable in intensity to the incident pump within the duration of the laser pulse. By analogy with the conventional SBS threshold, we can define an "onset threshold," which requires that the noise grow by a factor  $\exp(25)$  within the duration of the laser pulse:

$$\begin{aligned}
 M_1 &= M_{instab} \Rightarrow p = 0 \\
 M_1 &= M_{onset} \Rightarrow \exp(p t_{pulse} / \tau_B) = \exp(25) .
 \end{aligned}
 \tag{41}$$

By using Eq. (41) for our experiment, a growth rate  $p = 2.4/\tau_B$  is required. In Fig. 7 this growth rate (the onset threshold) occurs at more than 3 times the intensity of the instability threshold and increases with increasing cavity length. In this case the onset threshold is now a factor 5 less than the SBS threshold—substantially reduced, but not by as much as predicted by the instability threshold alone, and much closer to experimental observations.

We write  $t_{on}$  as the time delay before the loop produces an output. In the case of a short cavity, Fig. 7 shows that  $p$  depends linearly on intensity. For the onset threshold we can write:

$$\begin{aligned}
 p_{onset} t_{pulse} &\approx 25 \approx p_0(I_1 - I_{instab})t_{on} \\
 &\Rightarrow p_0 E_{on} \approx 25 + p_0 I_{instab} t_{on} ,
 \end{aligned}
 \tag{42}$$

where  $E_{on} = I_1 t_{on}$  can be thought of as an "onset energy," which is required before an output from the loop can be observed. As we increase the pulse energy, this will remain almost constant, decreasing slightly as the onset time decreases.

Figure 8 shows the instability threshold. In Fig. 9 we plot the onset threshold as a function of round-trip transmission coefficient for various values of  $f_0$ . Not surprisingly, the threshold increases as the overlap or transmission coefficient decreases. Although the instability threshold remains modest at the lowest values of  $f_0$  and  $T$ , the onset threshold becomes large. This is less of a problem with other materials having shorter phonon lifetimes.

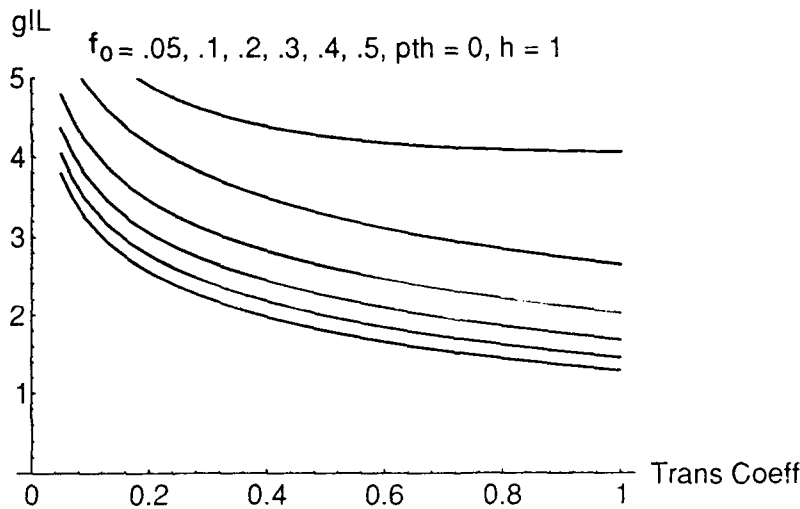


Fig. 8 — Instability threshold vs loop transmission coefficient for various overlaps

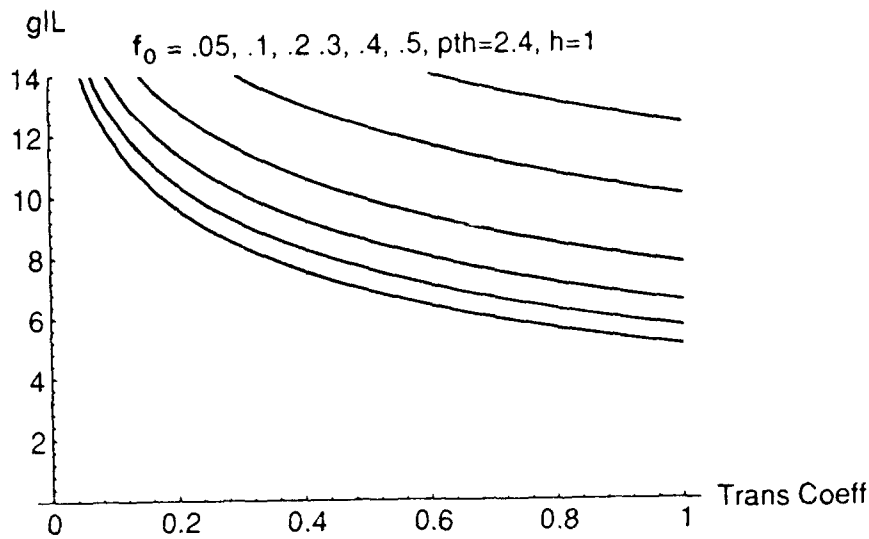


Fig. 9 — Onset threshold vs loop transmission coefficient for various overlaps

In Fig. 10 we consider the effect of varying the phase mismatch  $\Delta\phi$ . In the two diagrams we plot the instability threshold and detuning parameter for the case  $f_0 = 1$ ,  $h_1 = 1$ ,  $t_1 = t_2 = 0.8$ . This shows that the threshold is substantially increased when there is a significant phase mismatch. The frequency of the conjugate varies smoothly as the phase mismatch varies. If we increase the overlap  $f_0$  from 0.1 to 0.5 the same features are observed, with a reduced threshold, but the frequency detuning becomes more bent, becoming larger at the maximum phase mismatch values.

Figure 11 shows the contribution played by the Brillouin amplification. The upper of the three curves shows the onset threshold when only four-wave mixing is taking place (i.e., with  $h = 0$ , valid in the case of a large intersection angle when the Brillouin shifts are different in the two gratings). The middle curve corresponds to the case of Brillouin gain in the overlap region only but no auxiliary amplifier. The lower curve is for the case of a second Brillouin amplifier (i.e., with  $h = 0$ ;  $h = 1$ ,  $L_A = 0$ ; and  $h = 1$ ,  $L_A \neq 0$ ). The Brillouin amplifier makes only a small contribution to the value of the instability threshold, particularly when there is a high loop transmission coefficient.

We can examine the role of speckle enhancement and determine how it affects the growth rate. Figure 12 shows that the conjugate beam does experience an increased growth rate but that this is a somewhat smaller difference than the factor 2 observed in conventional SBS. This suggests that the discrimination between the conjugate and nonconjugate beams may not be as large as is the case in conventional SBS.

In Fig. 13, the difference in threshold with and without gain enhancement is seen to be greatest in the case of small overlap and low transmission around the loop. In the case of small overlap, the conjugate threshold stays almost constant as  $T$  drops from 100% to about 10%, while the nonconjugate threshold increases by 60%.



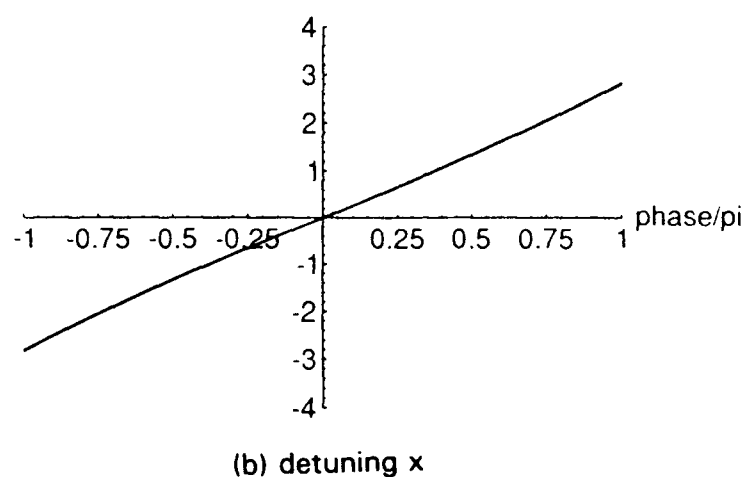
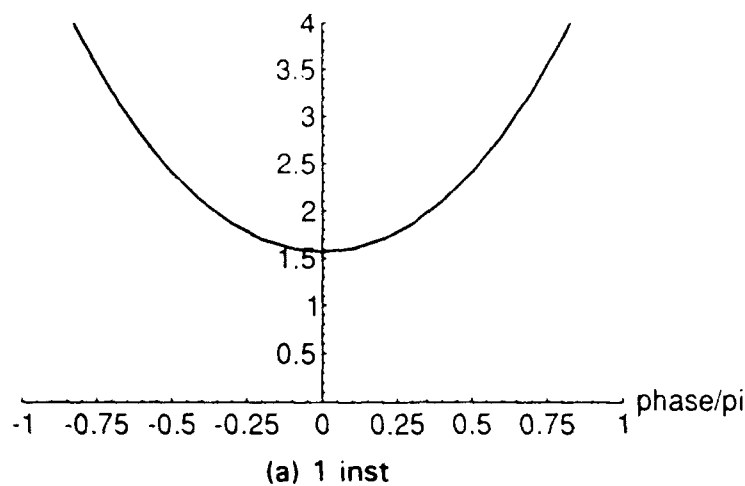


Fig. 10 — Instability (top) and detuning parameter (bottom)  
vs phase mismatch for  $f_0 = 1$ ,  $h_1 = 1$ ,  $t_1 = t_2 = 0.8$

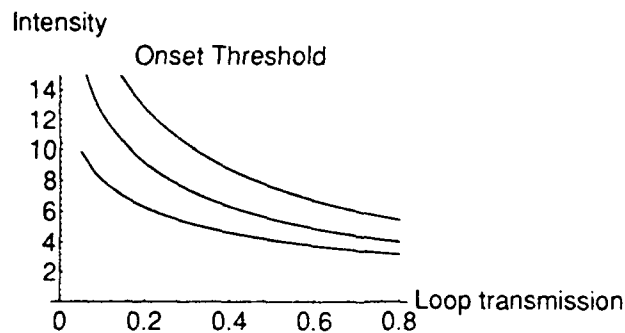


Fig. 11 — Onset threshold vs transmission coefficient  
Top curve — no Brillouin amplification (e.g., with large intersection angle)  
Middle curve — Brillouin amplification in overlap region only  
Bottom curve — Brillouin gain in overlap region and in second focal region

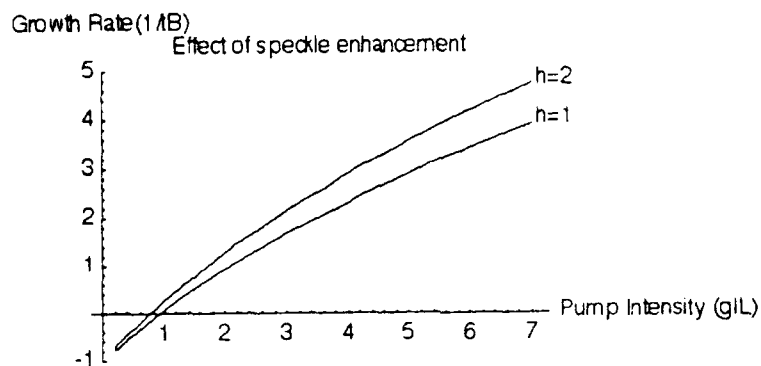


Fig. 12 — Effect of speckle enhancement on growth rate as function of pump intensity

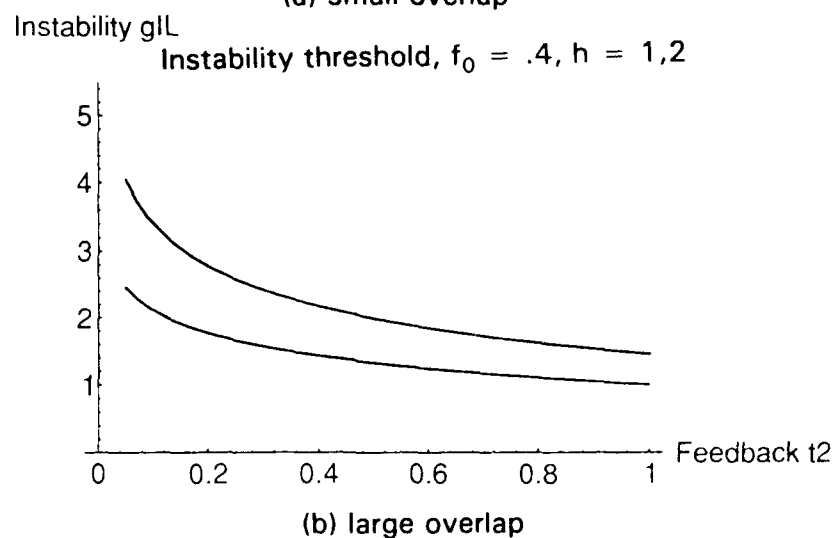
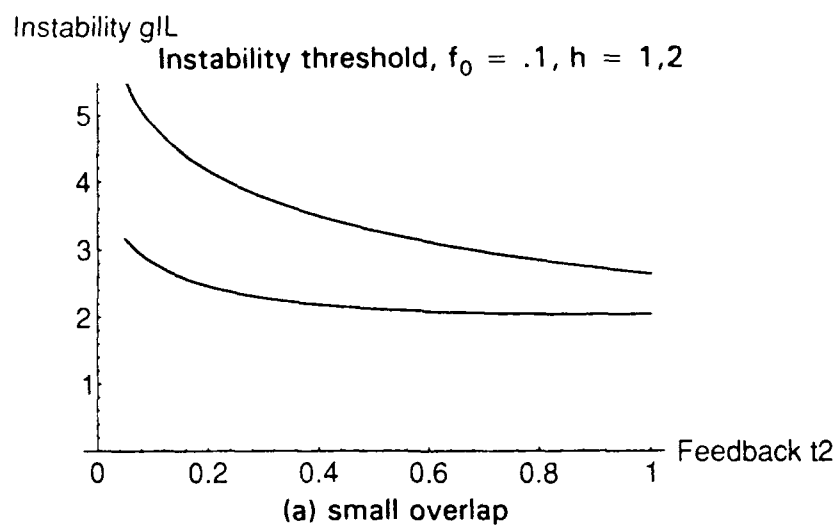


Fig. 13 — Instability threshold vs feedback; for small overlap (top) and large overlap (bottom graph). Lower curves depict the conjugate; upper curves depict the nonconjugate thresholds

### Steady State Theory

In the steady-state calculation we take all time derivatives to be zero and consider the six coupled equations derived from Eqs. (6) and (9):

$$\begin{aligned}
 \frac{\partial E_1}{\partial r} &= \frac{g}{2(1+ix_1)} \{(|E_2|^2 + |E_4|^2)E_1 + E_3E_4E_2^*\} \\
 \frac{\partial E_2}{\partial r} &= \frac{g}{2(1+ix_1)} \{(|E_1|^2 + |E_3|^2)E_2 + E_3E_4E_1^*\} \\
 \frac{\partial E_3}{\partial r} &= \frac{g}{2(1+ix_1)} \{(|E_2|^2 + |E_4|^2)E_3 + E_1E_2E_4^*\} \\
 \frac{\partial E_4}{\partial r} &= \frac{g}{2(1+ix_1)} \{(|E_1|^2 + |E_3|^2)E_4 + E_1E_2E_4^*\} \\
 \frac{\partial E_5}{\partial r'} &= \frac{-g}{2(1+ix_1)} |E_6|^2 E_5 \\
 \frac{\partial E_6}{\partial r'} &= \frac{-g}{2(1+ix_1)} \{(|E_5|^2 E_6)\}.
 \end{aligned} \tag{43}$$

It is practical to consider the case when  $x = 0$  and  $\Delta\phi = 0$ . The last two equations above can be solved immediately, leaving the four coupled equations. The four equations can be integrated numerically in the following manner. Firstly we note that the quantity  $C = |E_1|^2 - |E_2|^2 + |E_3|^2 - |E_4|^2$  is conserved. The equations are numerically integrated from  $r = L$  to  $r = 0$ , starting with estimates for  $E_1, E_2, E_3$ , and setting  $E_4 = 0$ . Given the values for  $E_2$  and  $E_3$  at  $r = L$ , the equations for the Brillouin amplifier can also be used to predict the values of  $E_5$  and  $E_6$  and hence  $E_4$  and  $E_2$  at  $r = 0$ . The selected values of  $E_2$  and  $E_3$  at  $r = L$  are then adjusted and the procedure repeated until the boundary conditions are met. At this time, a result for one value of  $E_1$  at  $r = 0$  is obtained. Once this has been obtained, the parameters are slowly varied to obtain an output intensity versus input (Fig. 14).

The curved line that stops as it approaches zero (where  $M_1 = 1.4$ ) is the output of the modeling ( $f_0 = 0.5$ ,  $T = 0.64$ ). (The modeling became unstable when  $M_1$  reached zero.) The straight line on the figure has a slope of 1 and crosses the horizontal axis at the instability threshold. The result shows that in the steady state regime the loop output has a slope efficiency of 100% (more than 100% near threshold) and implies that the steady state threshold is the same as the transient threshold predicted by theory.

Note that the above modeling requires no noise term, so that unlike SBS, the threshold does not depend on the level of spontaneous scattering. This also means that over long time scales the output will not be expected to vary as the result of noise-related fluctuations.

### LOOP EXPERIMENTS

The experiments were carried out at  $2.12 \mu\text{m}$  by using a Q-switched Ho:YAG laser and the apparatus shown in Fig. 15. The Ho laser consisted of a flashlamp pumped 5-mm-diameter  $\times$  66.5-mm rod in a 90-cm optical-path cavity with a  $\sim 2.5$ -mm-diameter transverse mode-selecting aperture. The  $2.1207\text{-}\mu\text{m}$  line was selected by using a 3-mm-thick quartz birefringent filter at the Brewster angle. This line was narrowed from  $\sim 30$  GHz down to  $\sim 0.6$  GHz by use of two intracavity uncoated etalons (6.4-mm sapphire

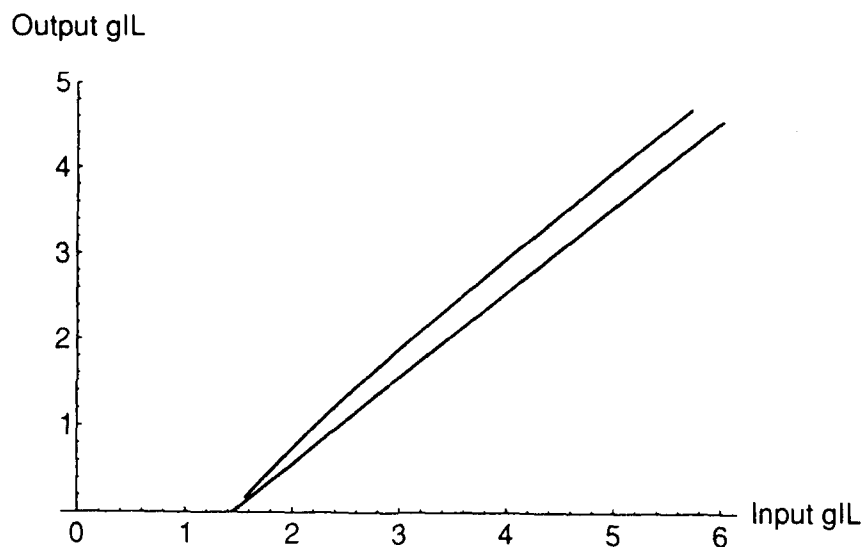


Fig. 14 — Steady-state plot of output vs input. The upper curve is the calculation for  $f_0 = 0.5$ ,  $T = 0.64$ . The lower is a straight line with slope 1 and crosses the axis at the instability threshold.

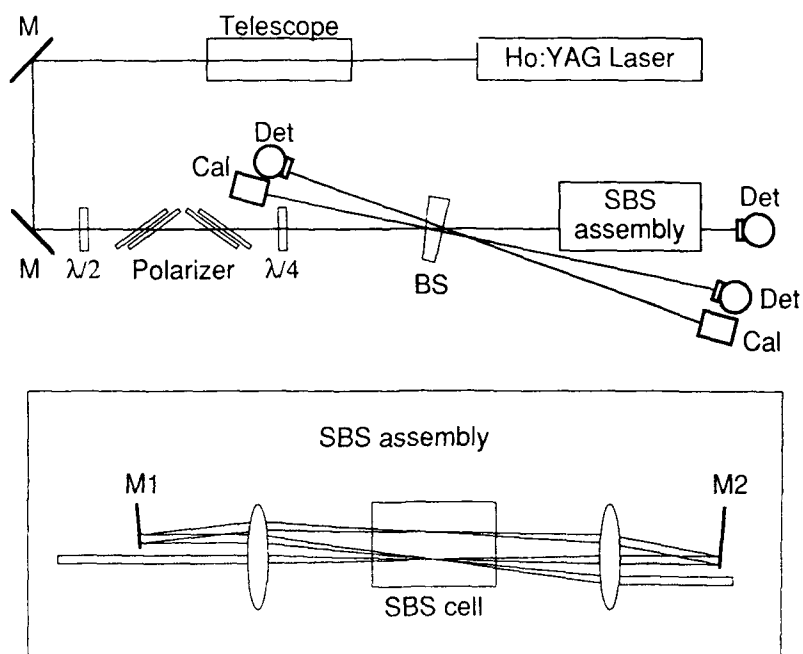


Fig. 15 — Schematic of loop-SBS experiments. The telescope provided an expanded waist at the input to the SBS assembly. M designates mirrors, Cal are pyroelectric calorimeters, Det are Ge:Au detectors, and BS is a wedged beamsplitter.

and 4.0-mm quartz). [The finesse for the sapphire etalon is 0.91 with a free spectral range (FSR) of 13.5 GHz; for the quartz it is 0.68 with a FSR of 24 GHz.] The cavity was Q-switched by using an acousto-optic modulator to produce pulses of up to 25 mJ, with a duration of ~210 ns at 1 Hz. Traces of the output pulse show strong axial mode beating, which could be averaged out electronically. A sample trace is shown in Fig. 16. Fourier transforms of the traces showed only  $c/2L$  axial mode frequency multiples present in the spectrum. The power spectrum changed from shot to shot and generally displayed 4 to 6 modes, consistent with the Fabry-Perot measurements.

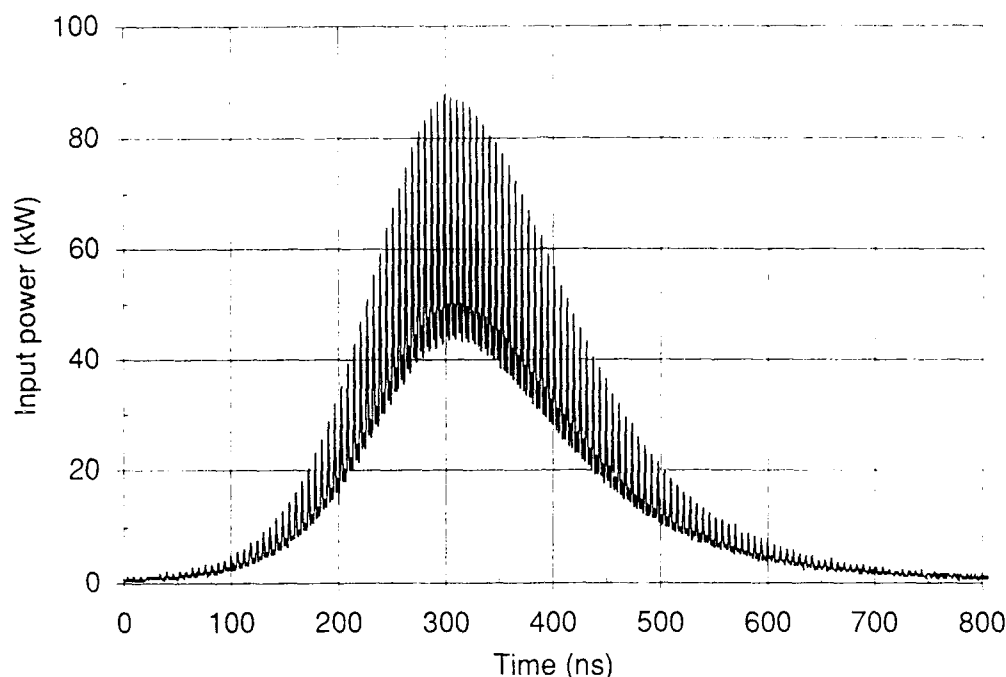


Fig. 16 — Sample trace of Ho laser output showing modulation resulting from axial mode beating

The output of the laser was directed through a collimating, beam-expanding telescope via beam-steering mirrors to a half-wave plate followed by a polarizer consisting of two ZnSe Brewster plates. This allowed the beam to be attenuated by rotating the half-wave plate. A quarter-wave plate produced circular polarized light that acted as an isolator to reduce feedback from backscattered light back into the oscillator. The backscatter extinction coefficient was approximately 10:1. When the half-wave plate was used to strongly attenuate the incident beam, the beam quality was degraded. This was probably the result of multiple reflections inside the polarizer.

The output from the isolator was directed through a CaF<sub>2</sub> wedge that reflected fractions of the pump beam and any conjugate to diagnostics. The diagnostics consisted of pyroelectric calorimeters and Au-doped Ge detectors that monitored the energy and intensity of the two beams. Additionally a third Au-doped Ge detector monitored the radiation transmitted by the Brillouin medium. The absolute power sensitivity of the fast detectors could be obtained by numerically integrating the area under a trace and relating this to the laser output measured at the same time.

As shown in Fig. 15, the laser beam was directed past mirror M1 to the first lens and focused into the Brillouin cell. The cell was sealed with CaF<sub>2</sub> windows and filled with CS<sub>2</sub> (Aldrich HPLC [high pressure liquid chromatography grade]). The length of the active medium was 10.7 cm. The transmitted beam was recollimated by the second lens and directed to dielectric mirror M2, which has 96% reflectivity. This was

tilted a few degrees from normal incidence and returned the beam to form a second focus a few mm to the side of the first. The transmitted beam was recollimated by the first lens and directed onto mirror M1, a gold-coated Ge etalon with 98% reflectivity. The reflection from this mirror was refocused by the first lens and overlapped the first focus.

The intersection angle between the two overlapping beams at the focus depends on the focal length of the first lens and the separation between the axes of the two beams at the lens. This separation is the same as the separation between the beam transmitted past the edge of mirror M1 and the beam reflected by it. Both lenses had focal lengths of 23.5 cm and mirrors M1 and M2 were positioned 16 cm from the lenses. As the tilt angle on mirror M2 was varied from 10 mrad to 70 mrad, the displacement between the centers of the two beams at mirror M1 varied from 2 to 3 mm.

### Alignment of the Loop

Mirror M1, which was polished on both sides flat and parallel within 10 arc sec, was on a kinematic mount that could be translated during the alignment procedure. In one position it reflected the pump beam before it reached the SBS cell, or it could be moved out of the way to transmit the beam after it had been reflected back from mirror M2. Thus two beams could be provided for alignment. These beams were reflected by the CaF<sub>2</sub> beamsplitter and refocused by a third lens to a graphite target at the focal plane where weak breakdown could be observed. The spacing between the two SBS lenses was adjusted to ensure that the foci of the two alignment beams were the same distance from the third lens. Mirror M1 was then tilted until the two focal spots overlapped. When they overlap here they also overlap in the Brillouin cell. Final adjustment was made of mirror M1 while monitoring the energy of the backscattered beam. This procedure was found to be quick, reproducible, and convenient.

### Energy Measurements

The input energy was varied, in one case by varying the laser flashlamp voltage and in the other case by varying the half-wave plate, and the resulting output was measured. The backscatter measurements were calibrated by using a 94% reflectivity copper mirror placed immediately in front of the loop. Measurements were made for the loop and with the pump beam blocked after it had passed through the cell once or twice, corresponding to single- or two-focus SBS. The results in Fig. 17 show that in all cases the backscattered signal was characterized by a threshold and a slope efficiency. The slope efficiency was 91% for the loop; 87% for two foci, and 72% for the single-focus case. The threshold for conventional SBS was 10.5 mJ; this dropped to 8.2 mJ for two-focus SBS. The threshold for the loop was 4.8 mJ. The maximum reflectivity was 64% for the loop, 36% for two-focus SBS, and 21% for single-focus SBS.

When the single-focus SBS threshold is used as the benchmark, the two-focus SBS scheme reduces the threshold by 1.3 and the loop reduces the threshold by a factor 2.2. The comparison between theory and experiment for the loop will be made later. However, in going from one-focus to two-focus SBS, we would expect the threshold to be reduced by a factor 1.8, after accounting for transmission losses ( $T \sim 80\%$ ). Because the laser operated on several axial modes, it was expected that the optical path between the two foci should be set to the laser cavity optical path length to within a small fraction of the overall coherence length ( $L_{\text{coh}} = c/\Delta\nu \approx 50$  cm). However, we found no significant effect in varying the focal separation.

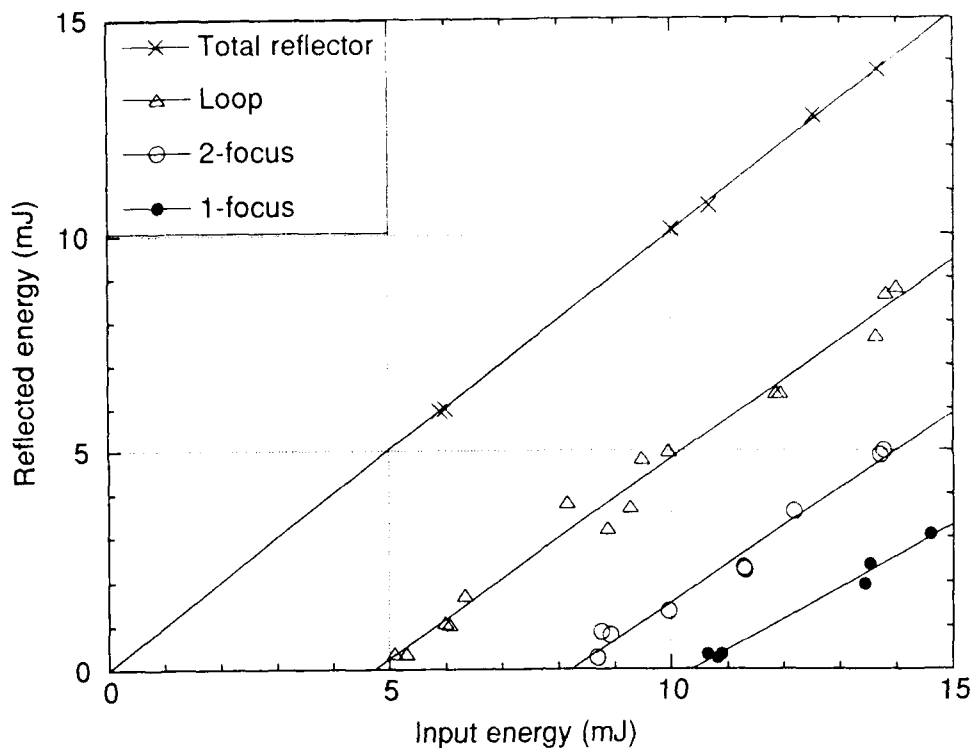


Fig. 17 — Plot of reflected energy vs input energy

### Intensity Measurements

Figure 18 is typical set of traces for the loop geometry. The transmitted beam has an initial transient spike followed by a region where the intensity is almost constant. The backscattered intensity switches on suddenly and follows the pump intensity. The traces can be absolutely calibrated by using the copper mirror and energy monitors. The transmitted and conjugate traces sum together to match the input trace to within a few percent over the whole pulse, indicating that all the power is accounted for.

In contrast, the set of traces, for a misaligned loop (Fig. 19) shows that the transmitted and backscattered beams are modulated and irregular.

Temporal data as in Fig. 18 can be used to calculate the reflectivity as a function of time (Fig. 20). This shows the sudden switch on of the conjugate beam and a power reflectivity nearly 90% at the highest pump powers.

Another way of presenting the data is to plot the backscatter intensity as a function of input intensity (Figs. 21 and 22). This approach, which converts the two traces into a Lissajous figure, was first used by Zel'dovich et al. [1]. The curve is traced in two passes: first on the rise of the input and again on the fall, with the transient behavior displayed during the initial part of the rise and steady state during the fall.

Figure 21 shows three sets of data taken at substantially different input energies. In each case, the initial transient behavior corresponds to loops near the origin where the output is zero while the input is increasing. After the reflected beam is established, the curves all lie close to the same curve. This curve is a straight line with a slope efficiency of ~100% and a threshold power of ~6 kW.

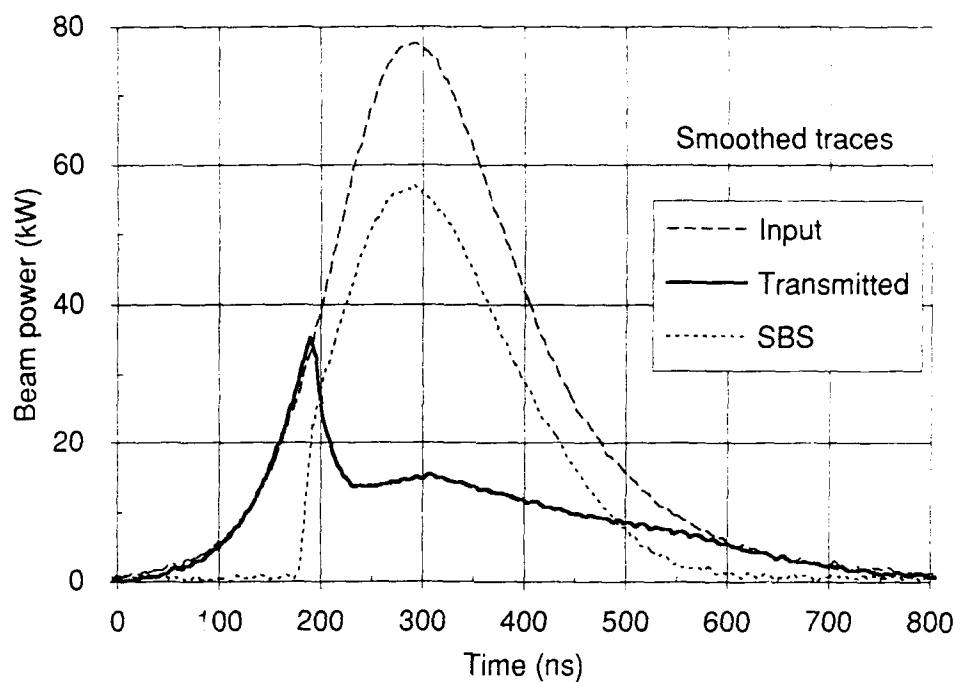


Fig. 18 — Typical temporal profiles of beams. The traces were electronically smoothed (removing appearance of mode beating) to display essential behavior.

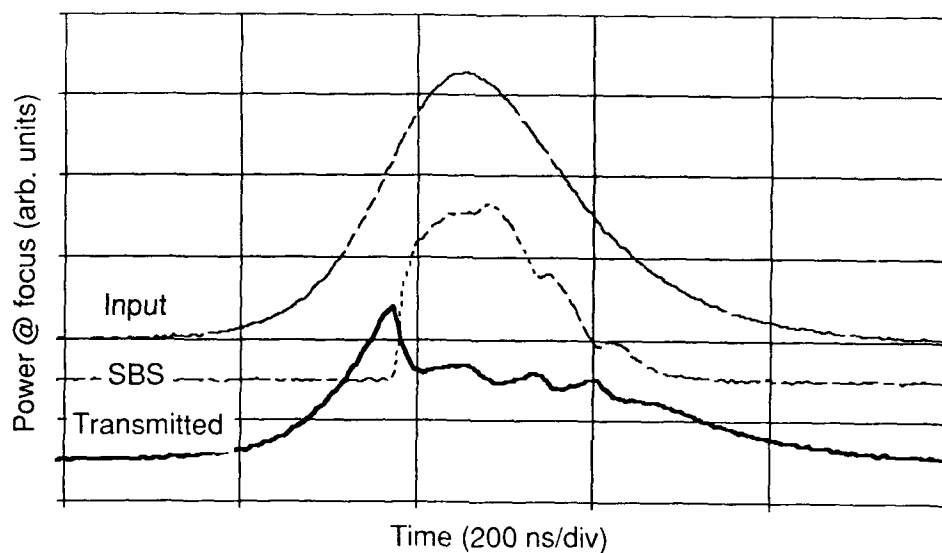


Fig. 19 — Temporal profiles showing slow modulation in reflected and transmitted beams for a misaligned loop. The traces were electronically smoothed (removing appearance of mode beating) to display essential behavior.



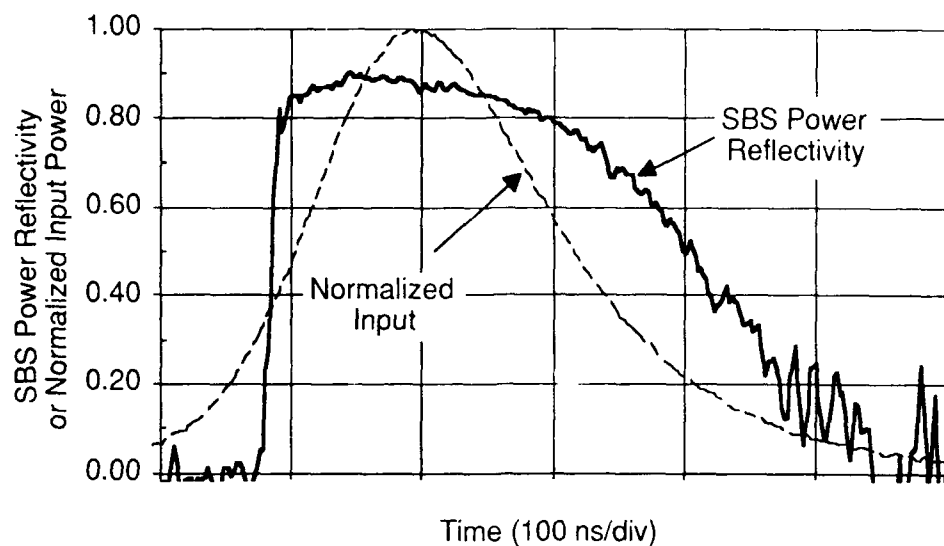


Fig. 20 — Reflectivity and normalized input power as function of time

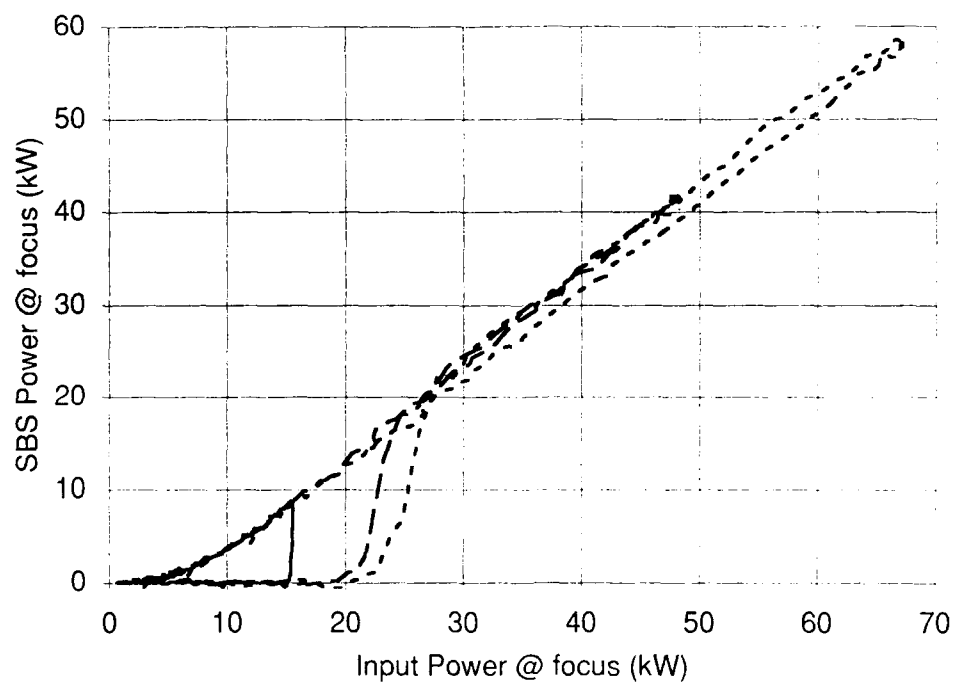


Fig. 21 — Reflected vs input power for three different input energies in the loop geometry. Straight line portions of the curves have slope efficiencies ~100%.

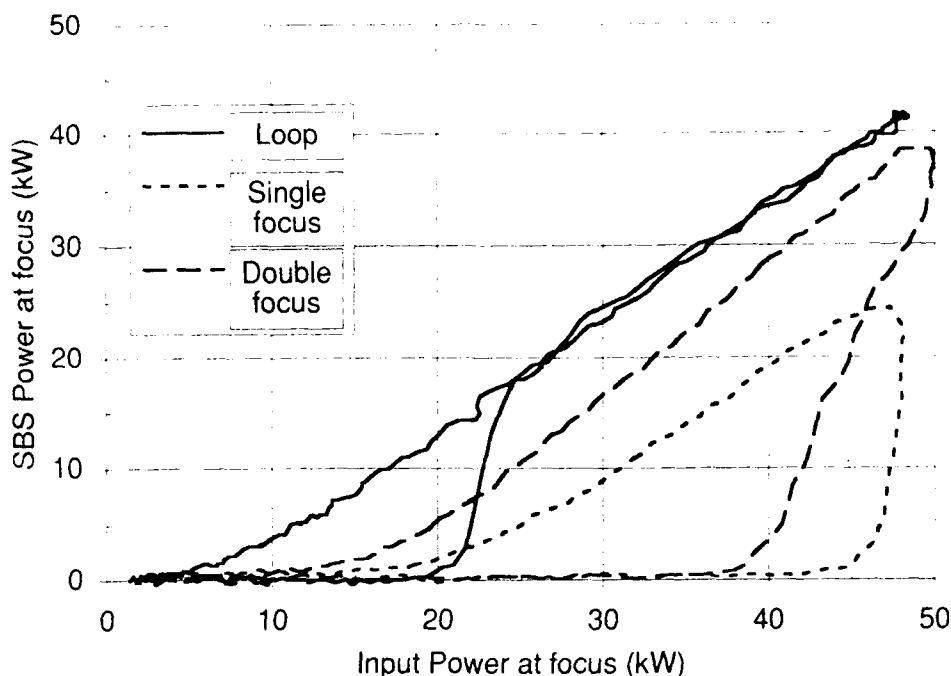


Fig. 22 — Sample plot of reflected vs input power for three different geometries

This experimental curve is similar in character to the modeling curve of Fig. 14. The main discrepancy is very close to the threshold, where the model predicted a sudden drop with a slope of greater than 100%. Two mechanisms could be responsible for this minor discrepancy. First, we note that the model neglected spontaneous noise. When this is included, the theoretical curve resembles more the curve above. Second, this low-reflectivity region corresponds to the regime where the time constant becomes very large so the acoustic wave and the reflectivity will change slowly and not reach full equilibrium.

Close to threshold where the signals are small, the curves are remarkably similar. At higher intensities, however, there is some spread in the data. The reasons for this are not certain but may be associated with self-focusing in the CS<sub>2</sub> or an artifact as the result of digital smoothing of the modulated oscilloscope traces. Figure 22 compares the behavior of the various geometries.

We commented in the theory section that the transient theory predicted an onset energy before the appearance of any backscattered beam. We can measure the onset energy by numerically integrating the input intensity up to the onset time. In Fig. 23 we show how we have defined the onset energy, and in Fig. 24 we plot onset energy vs input energy. It can be seen that the onset energy is indeed roughly constant. An evaluation of other parameters, such as the onset time or the input intensity when a backscatter signal appears, were all found to vary substantially with pulse energy.

A similar argument can be made for an onset energy for conventional SBS. In fact, the transient behavior of conventional SBS was found to be characterized by a similar onset threshold behavior (Fig. 25). The ratios of onset energies for the loop and the two-focus SBS to that of single-focus SBS are ~2.3 and 1.3 respectively.

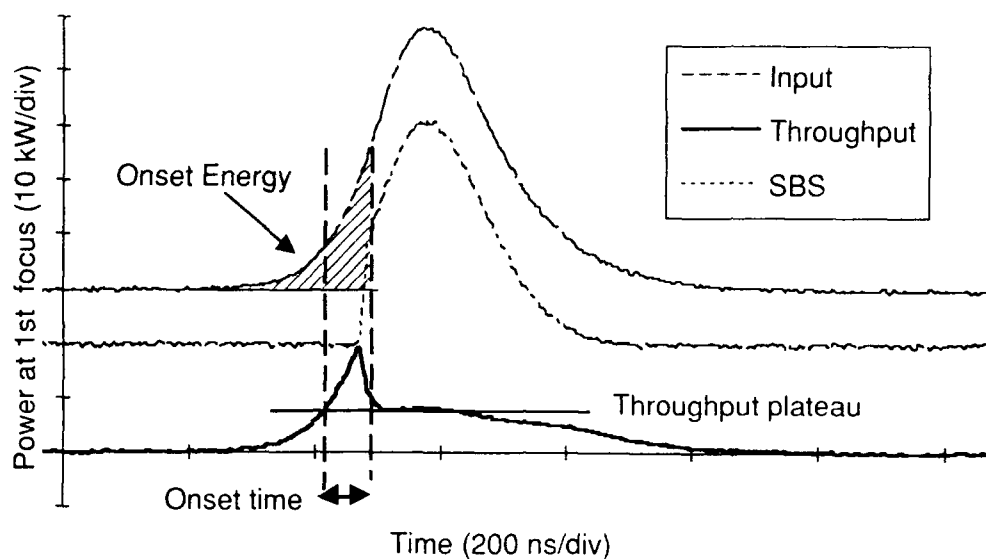


Fig. 23 — The onset energy, indicated by the hatched region, is defined as the time integral of the input power to the time when the reflected beam reaches 50% of its peak value. Since the reflected power rises so sharply, it made little difference whether we used 10% or 50% in the definition.

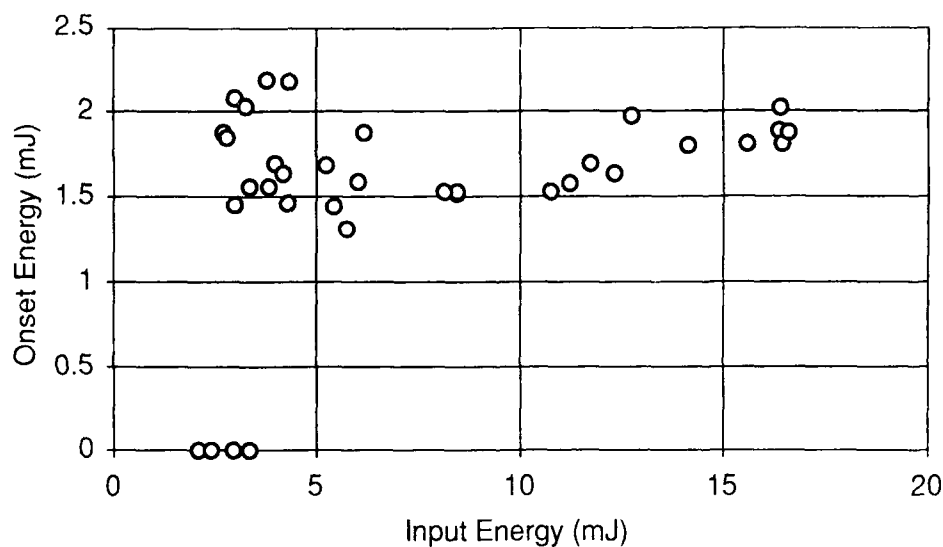


Fig. 24 — Energy for onset of stimulated scattering vs total input energy. Data were obtained by integrating the input pulse over time until the SBS signal reached 50% of its peak value.

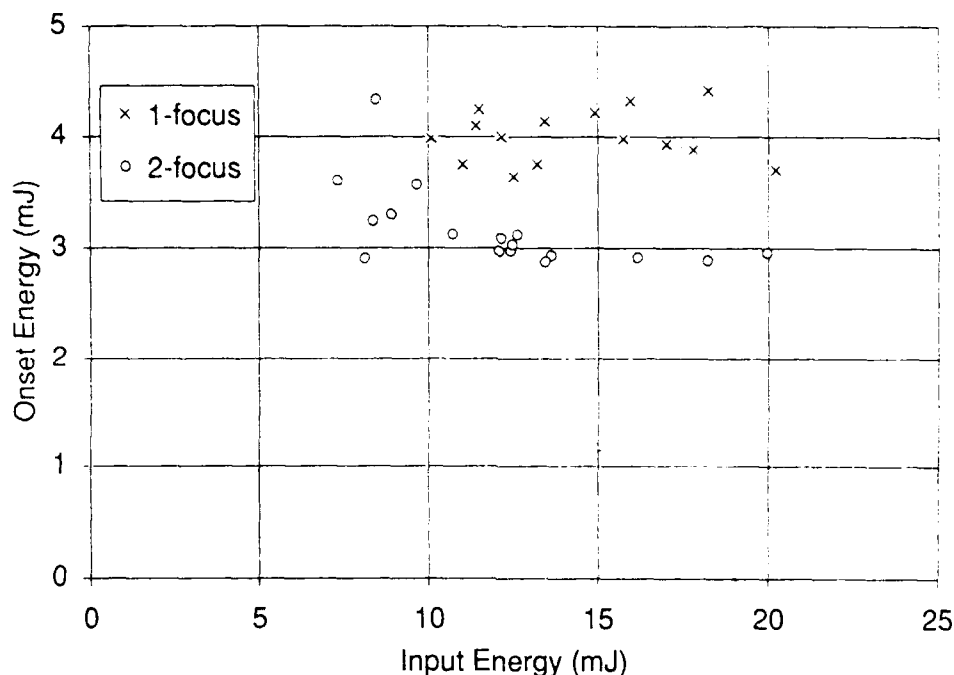


Fig. 25 — Experimental onset energy for SBS for a one- and two-focus geometry as a function of input energy

### Mirror Position

Experimentally, the most easily varied parameters are the transverse position of mirror M1 (Fig. 15) and the tilt angles of the mirrors. As mirror M1 is translated across the path of the input beam in one direction, it starts to obscure the input and hence reduce system efficiency. When it is moved in the other direction, it fails to intercept the beam coming from the second focus in the cell, and the effective transmission around the loop is reduced. These effects can be calculated and compared with experiment.

The effect of tilting the mirror M2 is to change the position of the return beam incident on the input beam. The beam is displaced, and this changes the overlap parameter. Additionally, part of this beam may fail to be reflected by the mirror M1, and this effectively reduces the loop transmission coefficient. The theoretical and experimental thresholds are shown in Figs. 26 and 27, respectively. Results show very little difference in threshold intensity but a slightly more noticeable change in the onset energy as the tilt angle is varied. It is evident that the discrepancy between theory and experiment is not particularly large. We noted a reduction in onset energy threshold of about 2.2 (Figs. 24 and 25), and we predict from theory a value of  $M = gIL = 8-10$  (Fig. 9), corresponding to a reduction of 2.5 to 3 in the threshold from the single-focus value.

Although no difference is apparent in intensity threshold with angle, some differences are observable in the traces. At large angles the transmitted and backscattered beams are smooth, but for small angles a characteristic modulation is observed, as in Fig. 19. This has been suggested [8] as being due to forward Brillouin scattering, and the modulation frequency is of the correct order of magnitude.

In the case of the loop, the longitudinal mode separation is given by  $\Delta k \Delta L = 2\pi$ , where  $\Delta k = k_2 - k_1$ ,  $k_1$ , and  $k_2$  are the wave vectors of the pump and Stokes beams respectively, and  $\Delta L$  is the change in loop length between longitudinal modes. For our experiment the calculated change in loop length to change by 1 mode was 11.1 cm. We adjusted the length to be 164 cm, 167 cm, and 169.5 cm.

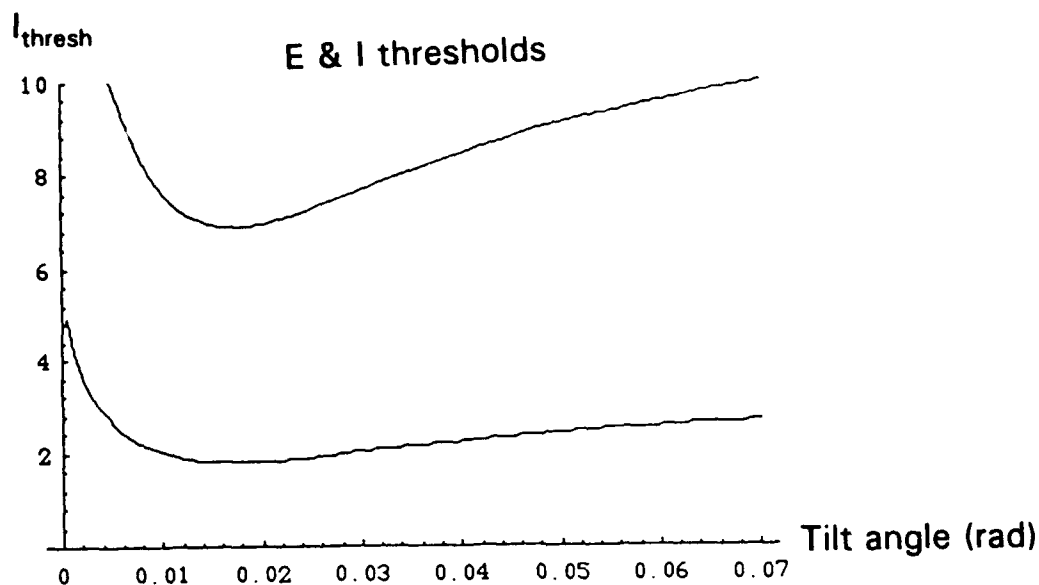


Fig. 26 — Calculated onset energy and intensity thresholds as function of tilt angle. The intensity threshold is given in terms of  $I_{\text{thresh}} = M = gIL$ ; the onset energy is calculated as the value of  $M$  assuming a square pulse with the characteristics given by Eq. (40).

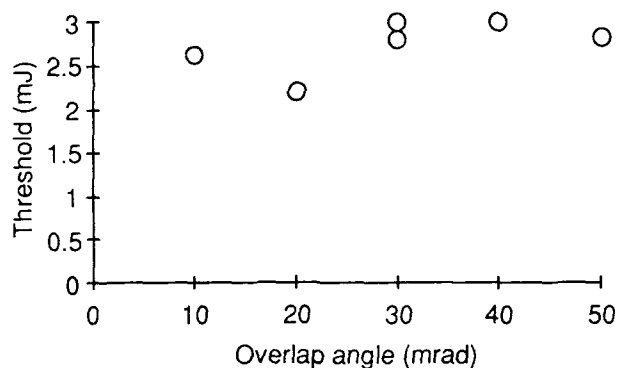


Fig. 27 — Measured energy threshold vs overlap angle. This has qualitatively the same shape as the curves in Fig. 26.

When it was 164 and 169.5 cm long, the SBS and throughput powers were as shown in Fig. 18. When the loop was varied to be 167 cm, the transmitted power was modulated as shown in Fig. 28 and the SBS was also modulated. The beat frequency was observed to be 14 MHz. This modulation was previously observed by Russian workers and was attributed to the excitation of higher order transverse modes [18].

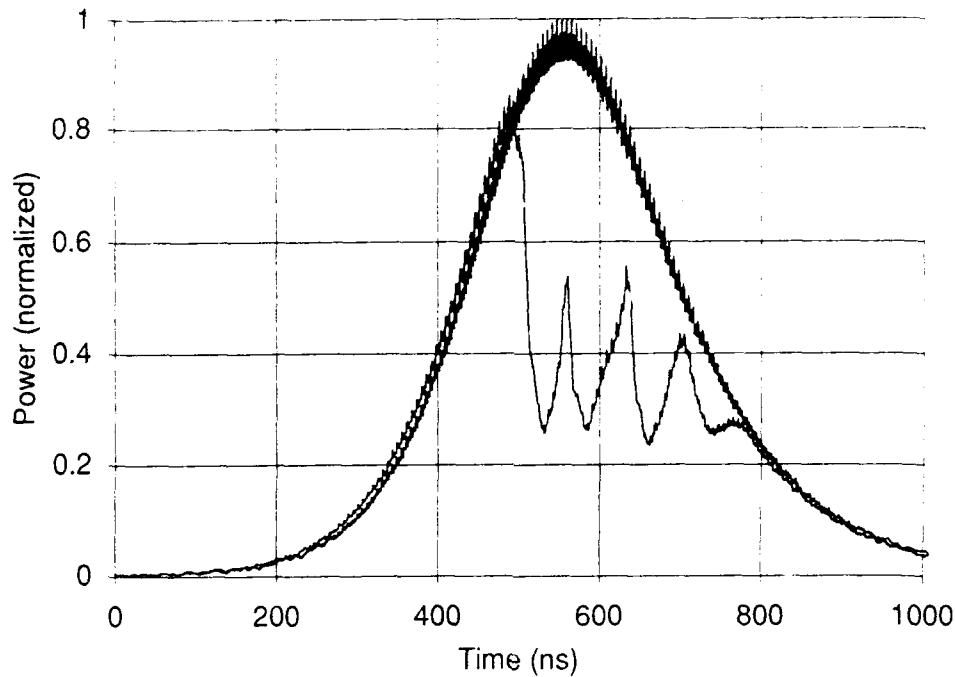


Fig. 28 — Input and throughput power when loop length is adjusted to make  $\Delta k L = (2n + 1)\pi$ . Modulation frequency is approximately 14 MHz

### Beam Quality

We first discuss the theoretical aspects of the lowest order Gaussian beam of waist  $\omega_0$  at  $z = 0$ . The radial intensity of the Gaussian beam of spot size  $\omega$  and on-axis intensity  $I_0$  can be written as

$$I(r) = I_0 \exp\left(\frac{-2r^2}{\omega^2}\right), \quad (44)$$

where the spot size is given in terms of the beam waist  $\omega_0$  and the parameter  $z_0$  by

$$\omega^2 = \omega_0^2 (1 + z^2 / z_0^2). \quad (45)$$

The full-angle divergence of this beam is given by

$$\theta_D = \lim_{z \rightarrow \infty} \frac{2\omega}{z} = \lim_{z \rightarrow \infty} \frac{2\omega_0}{z} \sqrt{1 + \frac{z^2}{z_0^2}} = \frac{2\omega_0}{z_0}. \quad (46)$$

In the case of a diffraction-limited beam, the parameter  $z_0$  becomes the Raleigh range  $z_R$  defined as

$$z_0 = z_R \equiv \frac{\pi \omega_0^2}{\lambda}. \quad (47)$$

This results in the product of the divergence times the beam waist having a value

$$\omega_0 \theta_D = \frac{2\omega_0^2}{z_R} = 2\omega_0^2 \frac{\lambda}{\pi \omega_0^2} = \frac{2\lambda}{\pi} = 1.35 \mu\text{m} \text{ for } \lambda = 2.12 \mu\text{m}. \quad (48)$$

The power transmission of a Gaussian beam through a centered circular aperture of radius  $r_0$  is given by

$$T(r_0) = \frac{2}{\pi\omega^2} \int_0^{r_0} 2\pi r \exp\left(\frac{-2r^2}{\omega^2}\right) dr = 1 - \exp\left(\frac{-2r_0^2}{\omega^2}\right). \quad (49)$$

If we focus a beam with a lens or mirror and measure the beam at the focal plane (not necessarily the beam waist), we measure the far-field divergence (since the intensity at the focal plane is an image of the intensity distribution at infinity). The beam diameter at this plane is independent of the position of the beam waist before the lens, although the position and size of the focal waist does depend on the position of the beam waist before the lens. This can be seen using the *ABCD* matrix formalism.

The *ABCD* matrix for a beam propagating a length  $L$ , being focused by lens with focal length  $f$ , and then propagating a length  $f$ , is given by :

$$\begin{bmatrix} A & B \\ C & D \end{bmatrix} = \begin{bmatrix} 1 & f \\ 0 & 1 \end{bmatrix} \begin{bmatrix} 1 & 0 \\ -\frac{1}{f} & 1 \end{bmatrix} \begin{bmatrix} 1 & L \\ 0 & 1 \end{bmatrix} = \begin{bmatrix} 0 & f \\ -\frac{1}{f} & 1 - \frac{L}{f} \end{bmatrix}. \quad (50)$$

Let  $q(z)$  be the complex radius of curvature at any point  $z$  given by

$$\frac{1}{q(z)} = \frac{1}{R(z)} - i \frac{\lambda}{\pi \omega^2(z)}, \quad (51)$$

where  $R(z)$  is the radius of curvature and  $w(z)$  is the spot size. The propagation law for this parameter is

$$q(z) = q_0 + z = z + i z_R, \quad (52)$$

with initial value

$$q_0 = i z_R = i \frac{\pi \omega_0^2}{\lambda}. \quad (53)$$

The propagated beam  $q_1$  is transformed as

$$q_1 = \frac{Aq + B}{Cq + D} = \frac{f}{\frac{-q}{f} + \left(1 - \frac{L}{f}\right)}, \quad (54)$$

$$\frac{1}{q_1} = \frac{-q}{f^2} + \frac{1}{f} - \frac{L}{f^2} = \frac{1}{R_1} - i \frac{\lambda}{\pi \omega_1^2}.$$

Now use Eqs. (52) and (53) for  $q$  and we have

$$\frac{-q_0 - z}{f^2} + \frac{1}{f} - \frac{L}{f^2} = \frac{1}{R_1} - i \frac{\lambda}{\pi \omega_1^2},$$

$$-i \frac{\pi \omega_0^2}{\lambda f^2} - \frac{z}{f^2} + \frac{1}{f} - \frac{L}{f^2} = \frac{1}{R_1} - i \frac{\lambda}{\pi \omega_1^2}. \quad (55)$$

Equating imaginary parts,

$$\begin{aligned}\frac{\pi\omega_0^2}{\lambda f^2} &= \frac{\lambda}{\pi\omega_1^2}, \\ \omega_1 &= \frac{\lambda f}{\pi\omega_0}.\end{aligned}\tag{56}$$

Thus the beam size in the focal plane is independent of the position of the waist and depends only on the wavelength, focal length, and waist size before the lens. Now use Eq. (48) and we have

$$\begin{aligned}\omega_1 &= \frac{\lambda}{\pi} \frac{f}{\omega_0} = \frac{\omega_0 \theta_D}{2} \frac{f}{\omega_0} = \frac{\theta_D f}{2}, \\ \theta_D &= \frac{2\omega_1}{f}.\end{aligned}\tag{57}$$

Thus the full-angle divergence of the beam is given simply by the beam diameter in the focal plane divided by the focal length of the lens.

If a beam is not diffraction-limited, then there is no general form for the beam. We briefly mention two different examples. In one case we may have a beam in which a substantial part has a Gaussian profile, and some residual fraction has a much larger diameter, forming a pedestal on which the central Gaussian lobe appears to stand. This lobe may have low intensity but contain a substantial fraction of energy.

A second possible situation is that the near and far field may appear Gaussian, but  $z_0$  may be smaller by a factor  $Q$  than  $z_R$ , i.e.,  $z_0 = z_R / Q$ . Then the divergence of this beam, using Eq. (46), is

$$\theta_D = \frac{2\omega_0}{z_0} = \frac{2\omega_0}{z_R/Q} = Q \frac{2\omega_0}{z_R} = Q(\theta_D)_{DL},\tag{58}$$

where  $(\theta_D)_{DL}$  is the divergence of a diffraction-limited beam with the same waist, i.e., we obtain a divergence increased by a factor  $Q$ , which can be taken as a measure of beam quality. Note that this is an empirical description rather than a solution.

Experimentally, a measure of the beam quality was obtained by measuring the waist before the focusing mirror (the near field) and the beam size in the focal plane (the far field), i.e., 401 cm from a 401-cm focal length mirror. We used Eq. (57) to determine the divergence. Measurements were made both by using a pyroelectric array and by measuring the transmission of a series of apertures ("energy in a bucket").

By using the energy in a bucket technique we found that in the near field, 97% of the input beam was in a Gaussian distribution with a value of  $2\omega_0 = 3.5$  mm. In the far field, more than 98% of the energy was in Gaussian profile with  $2\omega = 3.4$  mm. The data and the fits to Eq. (49) are shown in Figs. 29 and 30. When the loop was operated, more than 97% of the backscattered energy in the near field was in a Gaussian beam with  $2\omega_0 = 3.5$  mm. In the far field, 97% of the energy was in a Gaussian profile with  $2\omega = 3.3$  mm. The fidelity was taken as the ratio of the loop-reflected energy transmission to the input transmission of the aperture. These measurements were reproducible, both close to threshold and well above threshold. The data and the fits are shown in Figs. 31 and 32.



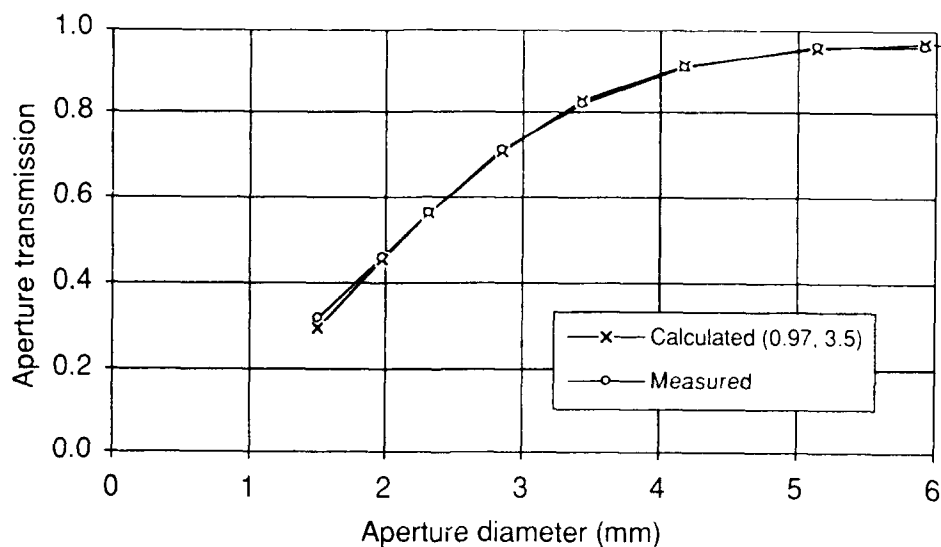


Fig. 29 — Energy-in-bucket measurements for the input near field. The calculated points are a Gaussian fit to the data, assuming 97% of the beam in a Gaussian distribution and a value of 3.5 mm as twice the waist.

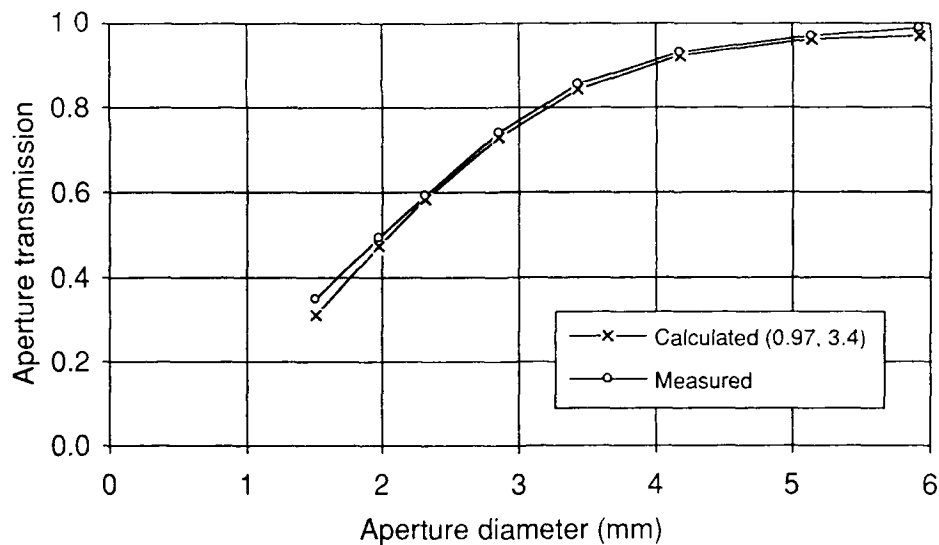


Fig. 30 — Energy-in-bucket measurements for the input far field. The calculated points are a Gaussian fit to the data, assuming 97% of the beam in a Gaussian distribution and a value of 3.4 mm as the beam diameter in the focal plane.

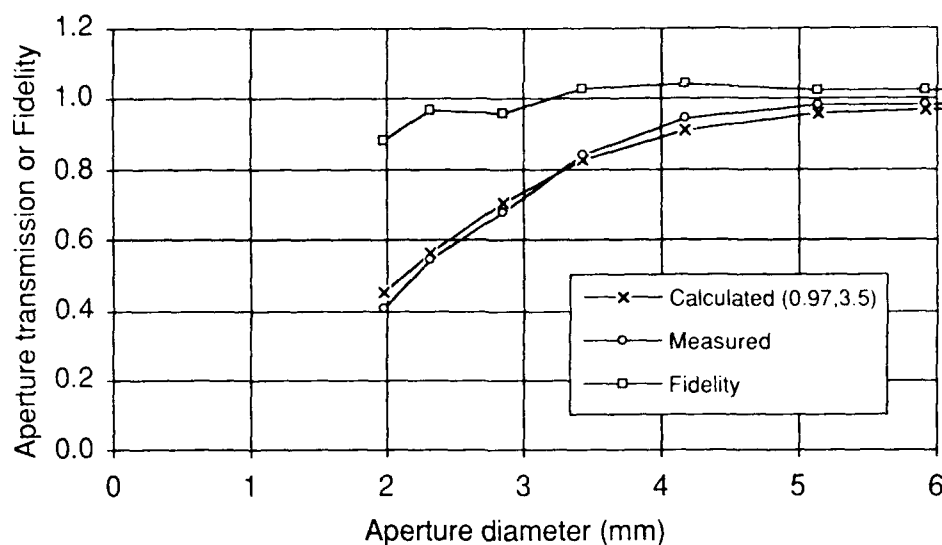


Fig. 31 — Energy-in-bucket measurements for the loop reflection near field. The calculated points are a Gaussian fit to the data, assuming 97% of the beam in a Gaussian distribution and a value of 3.5 mm as twice the beam waist. The fidelity was taken as the ratio of the measured loop-reflected energy transmission to the transmission of the aperture for the input beam near field.

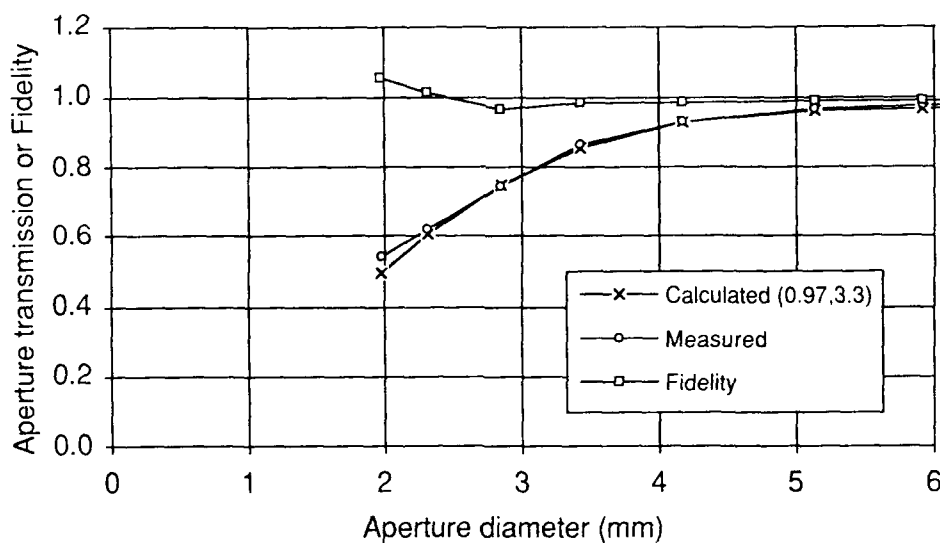


Fig. 32 — Energy-in-bucket measurements for the far field of the loop reflection. The calculated points are a Gaussian fit to the data, assuming 97% of the beam in a Gaussian distribution and a value of 3.3 mm as the beam diameter in the focal plane. The fidelity was taken as the ratio of the measured loop-reflected energy transmission to the input transmission of the aperture.

For comparison, similar measurements were made with the single-focus SBS (Figs. 33 and 34). More than 97% of the backscattered energy in the near field was in a Gaussian beam with  $\omega = 4.3$  mm. In the far field, 97% of the energy was in a Gaussian profile with  $\omega = 4.0$  mm.

Next, an aberrator plate (a NaCl window that had been wet with water and roughly repolished) was placed immediately in front of mirror M1. To measure the effect of the aberrator, the incident light was reflected by a copper mirror. Clear structure was seen in the near field but no noticeable intensity was seen outside a radius of  $\sim 3.5$  mm. Near-field energy in a bucket was not measured in this case. In the far field a highly structured speckle pattern was observed. Energy-in-a-bucket measurements showed the pattern to fit approximately a Gaussian profile, with a diameter in the focal plane of  $\sim 17$  mm (Fig. 35). When the loop-SBS system was operated with the aberrator in the same position, about 78% of the energy was observed to be in a Gaussian profile with a  $2\omega = 4.5$  mm (Fig. 36).

The fidelity of the conjugate beam is often defined by measuring the transmission of the input through a spatial filter and then measuring the transmission of the conjugate through the same aperture. The fidelity is taken to be the ratio of the two measurements. We plotted fidelity as a function of aperture and obtained a value of 0.55 to 0.78. At a diameter of 4 mm (corresponding to 86% transmission of the pump beam in the far field), the fidelity was about 65%.

## THEORY OF THE RING-SBS SCHEME

The theory of the ring-SBS scheme was first analyzed by Wong and Damzen [10]. We review this theory, extend it to take into account the effect of frequency detuning, and discuss transient behavior. In practice the theory for the transient ring is very similar to the theory of the auxiliary cavity.

We first discuss the steady state behavior. We consider a Brillouin amplifier in a cavity with a partially transmitting mirror having transmission coefficient  $T$  and a transmission coefficient around the ring of  $R = r^2$ , where  $r$  is the amplitude transmission coefficient. The equations for the Brillouin amplifier are

$$\frac{\delta E_1}{\delta r} = -\frac{g}{2(1+ix)} |E_2|^2 E_1 \quad \text{and} \quad \frac{\delta E_2^*}{\delta r} = -\frac{g}{2(1+ix)} |E_1|^2 E_2^*, \quad (59)$$

which become

$$\frac{\delta I_1}{\delta r} = \frac{-g}{1+x^2} I_1 I_2 = \frac{\delta I_2}{\delta r}. \quad (60)$$

This can be solved by using  $I_1(r) - I_2(r) = C$ , where  $C$  is a constant. The solution is

$$I_2(r) = \frac{I_2(0)[I_1(0) - I_2(0)]}{I_1(0) \exp\left\{\frac{g}{(1+x^2)} [I_1(0) - I_2(0)] r\right\} - I_2(0)}. \quad (61)$$

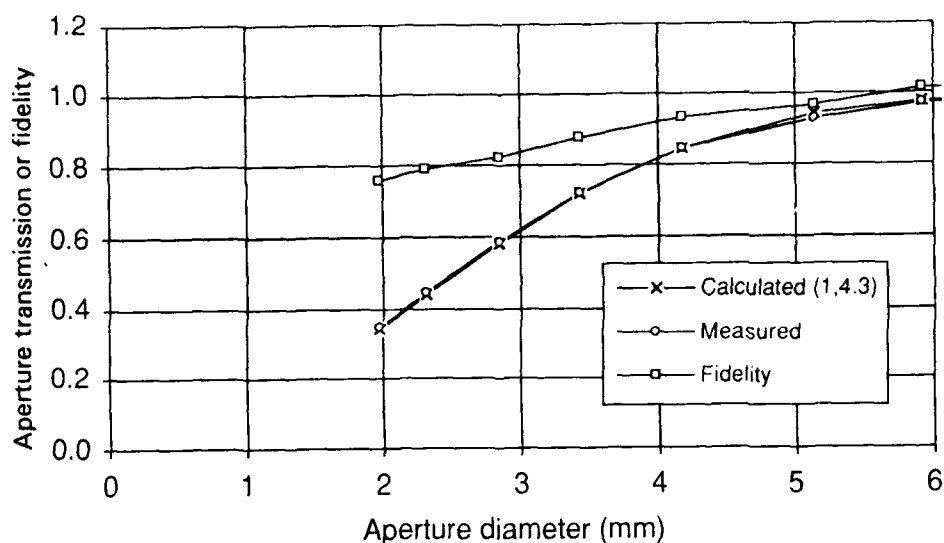


Fig. 33 — Energy-in-bucket measurements for near-field single-focus SBS. The calculated points are a Gaussian fit to the data, assuming 100% of the beam in a Gaussian distribution and a value of 4.3 mm as twice the beam waist. The fidelity was taken as the ratio of the measured reflected energy transmission of the aperture to the input transmission.

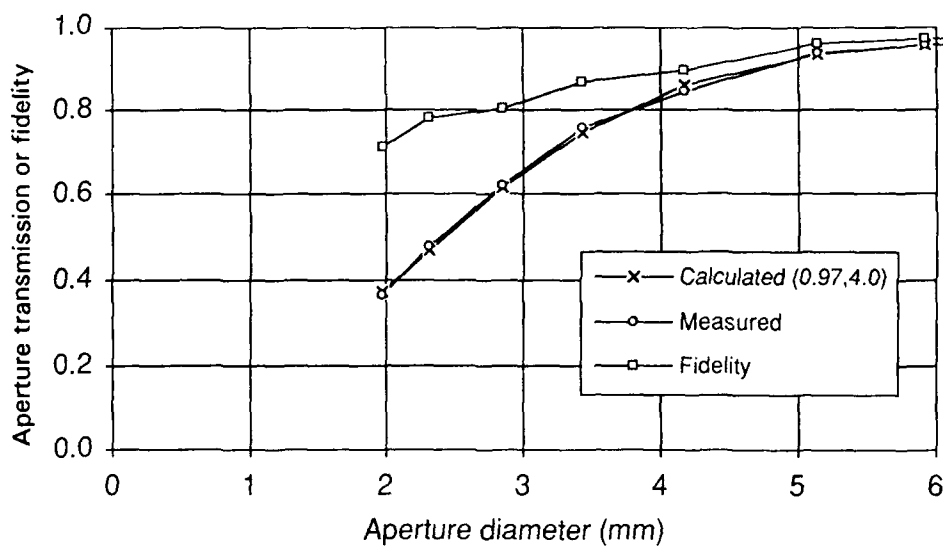


Fig. 34 — Energy-in-bucket measurements for far-field single-focus SBS. The calculated points are a Gaussian fit to the data, assuming 97% of the beam in a Gaussian distribution and a value of 4.0 mm as the beam diameter in the focal plane. The fidelity was taken as the ratio of the measured reflected energy transmission of the aperture to the input transmission.

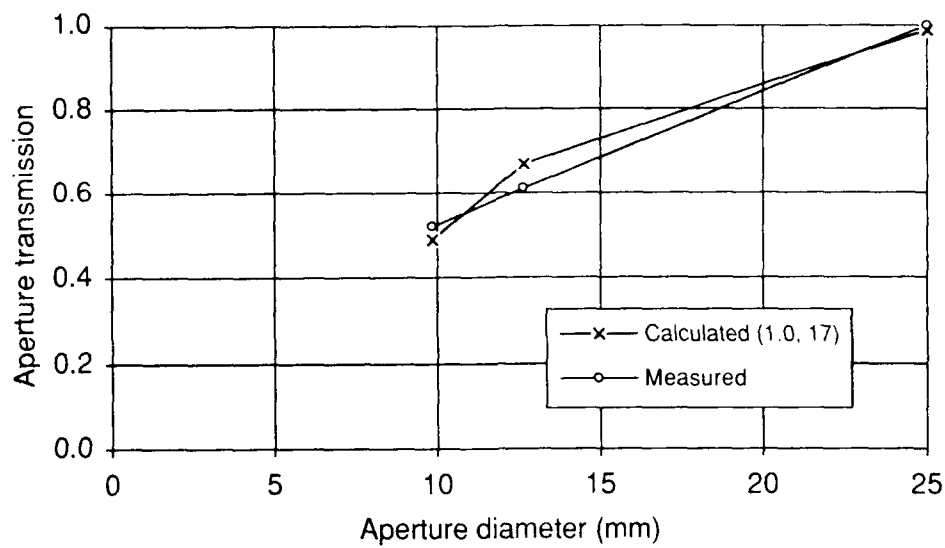


Fig. 35 — Energy-in-bucket measurements in far-field for reflection of aberrated beam reflected from flat mirror. The calculated points are a Gaussian fit to the data, assuming 100% of the beam in a Gaussian distribution and a value of 17 mm as the beam diameter in the focal plane.

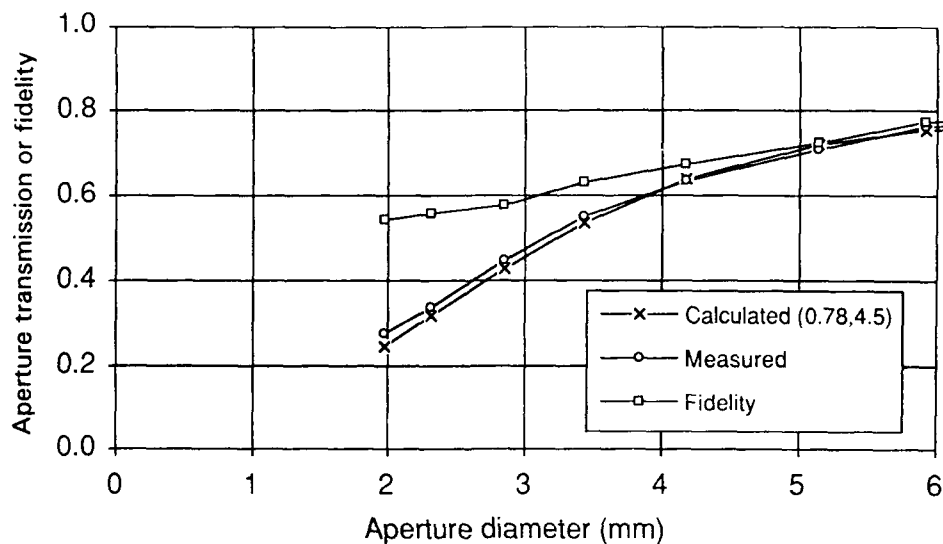


Fig. 36 — Energy-in-bucket measurements in far-field for reflection of aberrated beam reflected from loop SBS system. The calculated points are a Gaussian fit to the data, assuming 78% of the beam in a Gaussian distribution and a value of 4.5 mm as the beam diameter in the focal plane.

This expression can then be used to solve the equation for  $E_2^*$ , giving

$$E_2^*(L) = E_2^*(0) \exp\left\{\frac{-g(CL+J)}{2(1+x^2)}\right\} \exp\left\{\frac{ixg(CL+J)}{2(1+x^2)}\right\}, \quad (62)$$

where

$$J = \log\left\{\frac{I_1(0) \exp\left\{\frac{gCL}{1+x^2}\right\} - I_2(0)}{I_1(0) - I_2(0)}\right\}. \quad (63)$$

This can be written as

$$E_2(L) = E_2(0) \gamma_2 \exp\{i\phi_{B2}\}, \quad (64)$$

where the real part is gain and the imaginary part is a Brillouin-induced phase shift. We now consider the boundary conditions for the ring

$$E_2(0) = rE_2(L) \exp\{i\phi_S\} \quad (65)$$

$$\phi_S = k_2 L_R = \omega_2 L_R / c = (\omega_1 - \omega_B) L_R / c - x\delta\omega_0 L_R / c = \phi_{20} - x\delta\omega_0 L_R / c.$$

If we substitute this in the equation for the Brillouin amplifier we obtain

$$\phi_{20} - x\{\delta\omega_0 L_R / c - \log(1/r)\} = 2n\pi \quad (66)$$

or

$$x = \frac{2n\pi - \phi_{20}}{\{\delta\omega_0 L_R / c - \log(1/r)\}}. \quad (67)$$

The first term in the denominator is a mode pulling term and the second is a Brillouin-induced phase shift. An equation similar to this was proposed by workers at TRW [30]. It emphasizes that the degree of detuning is determined by the random phase shift around the cavity. In our case, the cavity has an effective value of 0.019 for  $r^2$ , and  $x$  can have a maximum value of  $x = 1.98$  when  $\phi_{20} = \pi$ .

The boundary condition also gives

$$\gamma_2^2 = \frac{1}{r^2} = \log\left\{\frac{I_1(0) \exp\left\{\frac{g[I_1(0) - I_2(0)]L}{1+x^2}\right\} - I_2(0)}{I_1(0) - I_2(0)}\right\}. \quad (68)$$

$I_1(0)$  is approximately given by  $TI_{in}$  and  $x$  is determined by the above, so  $I_2(0)$  is determined. By using this equation we can calculate the threshold power as a function of the random variable  $\phi_{20}$ , which may vary over  $\pm\pi$ .

The threshold  $\{I_1(0) - I_2(0)\}$  shows a large variation in threshold (Fig. 37). In fact the predicted variation in threshold is even larger than that observed.

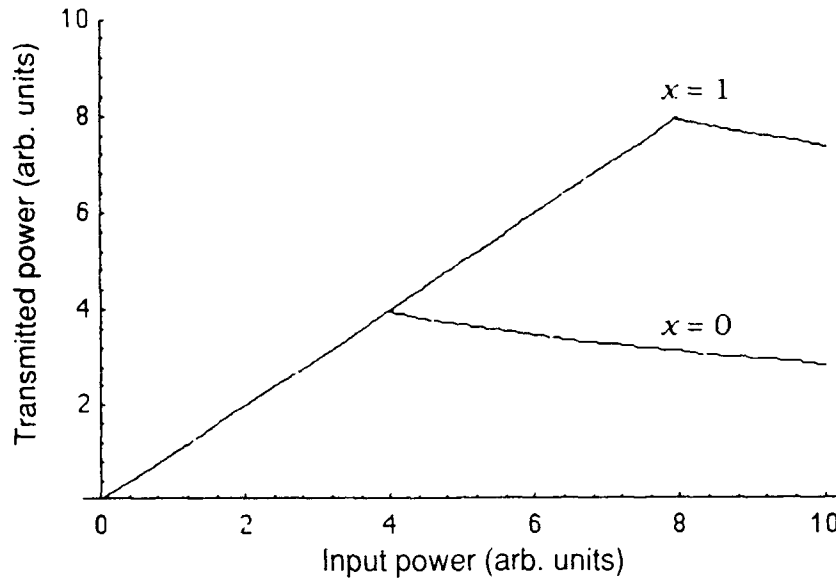


Fig. 37 — Power transmitted through ring in steady state regime. Lower curve corresponds to case when cavity mode is at center of Brillouin gain, i.e.,  $\phi_{20} = 0$ ,  $x = 0$ . Upper curve corresponds to cavity length such that mode is detuned from resonance, i.e.,  $x = 1$ .

To a first approximation, the ring can be alternatively considered as a loop where the overlap parameter is 1 and the feedback coefficient is small. In Fig. 38 we plot the threshold of the ring as a function of transmission coefficient and overlay this with the threshold of the loop. This shows that the loop is perhaps a factor 2 higher in threshold. However as discussed earlier, the loop is much less sensitive to the size of phase shift around the cavity.

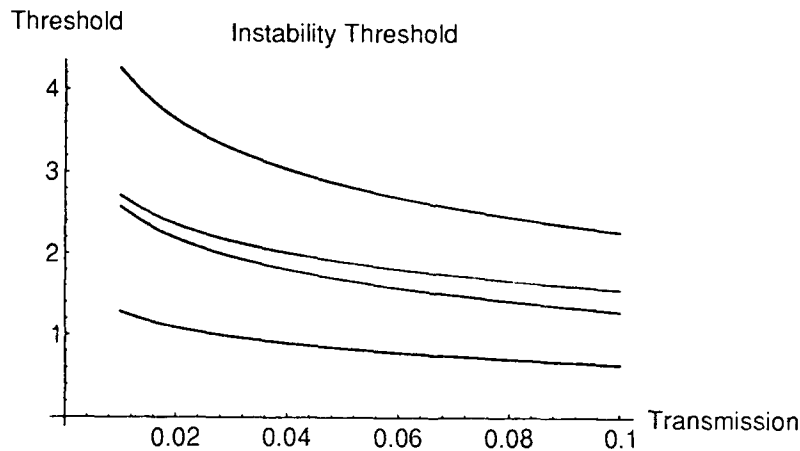


Fig. 38 — Top two traces: Instability threshold for a loop vs transmission, with overlap factor  $f_0 = 1$ . (Top trace: no gain enhancement; second trace from top: loop with gain enhancement. Vertical scale is in units of  $gIL$ . Lower two traces: Instability threshold for a ring vs transmission coefficient. Bottom trace: with gain enhancement; second trace from bottom: without gain enhancement.)

We note that the model of a ring-SBS scheme treats the system as a resonator, with the output of the Brillouin amplifier being fed back into itself. This can only be valid in the three-dimensional world if the cavity can be described as having self-consistent orthogonal modes. This concept suggests that the modes will become more extended when there are aberrations in the cavity and in turn would predict that the threshold will rapidly increase. Furthermore, if there are substantial aberrations in a ring cavity (such as were discussed by TRW workers [30]), then the wavefronts of the input beam after the second pass through the SBS cell will be substantially different from the wavefronts after the first pass. This also suggests that interference between the beam on the first and second pass plays a role in determining the spatial structure of the output. These two issues raise problems when the "ring-SBS" scheme is treated as a ring resonator, but it is less of a problem if the ring is treated as a particular case of the loop scheme.

## RING EXPERIMENTS

Figure 39 shows the experimental arrangement. It is similar to the loop discussed previously, but the first high-reflectivity mirror is replaced with a 3% reflectivity  $\text{CaF}_2$  wedge. Both this and the second high-reflectivity mirror were placed at the focal plane of the respective lenses. This provided a ring that was slightly larger than the loop described in the earlier experiments. To ensure that the temporal coherence criterion was met, the cavity length of the laser had to be changed and matched to the ring length. This was done and the birefringent filter and etalons were adjusted to optimize the performance of the laser, although the spectral characteristics were not reexamined with the scanning Fabry Perot etalon.

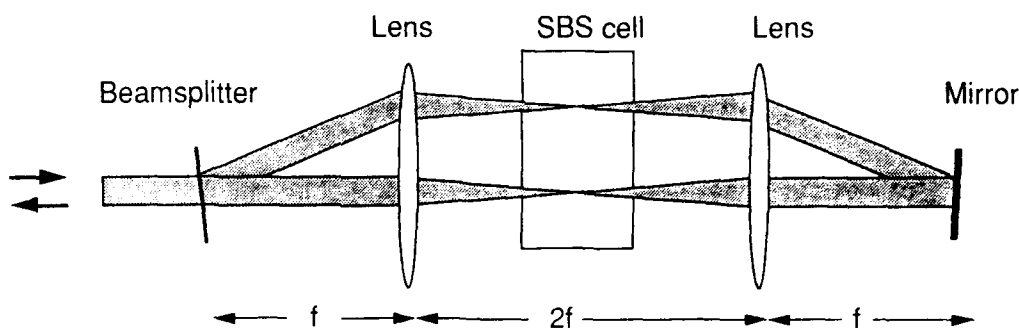


Fig. 39 — Experimental arrangement for ring SBS

In the ring arrangement, light incident on the second high-reflectivity mirror is imaged to overlap on the beamsplitter with the input beam. Alignment consists of adjusting the orientation of the beamsplitter; this is carried out in the same way as described for the loop.

The ring was initially set to be 200 cm round trip. Figure 40 shows SBS output energy vs input energy. As in the case of the loop scheme, the results were compared with the case of the single- and two-focus SBS cases. Comparing this with Fig. 17 shows that the threshold for single- and two-focus SBS are substantially the same as was observed earlier in the loop experiments. This suggests that the spectral properties of the laser are similar to those of the earlier experiments.

The threshold energy of the ring was significantly less than in the loop experiments. The ring had a threshold of 3 mJ compared to 4.8 mJ for the loop threshold.



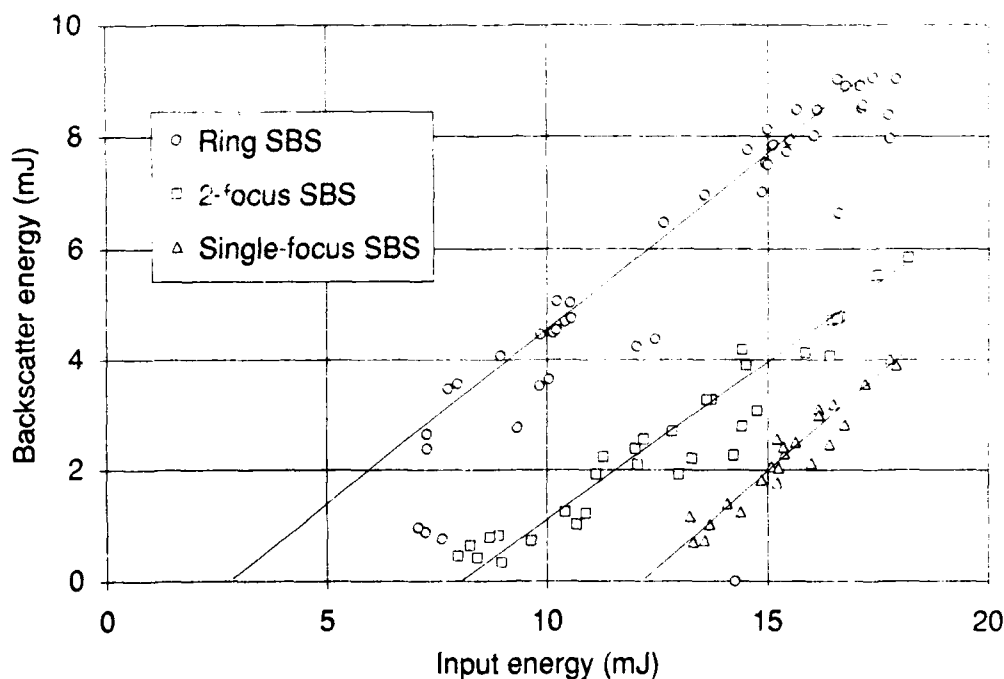


Fig. 40 — SBS energy vs input energy

We also measured the throughput and SBS powers in a series of experiments. Figure 41 shows sample traces. The studies showed that the dynamics and typical shape of the SBS and throughput pulses were very similar to those observed in the loop scheme, but the shot-to-shot variation was much larger than had been observed in the case of the loop.

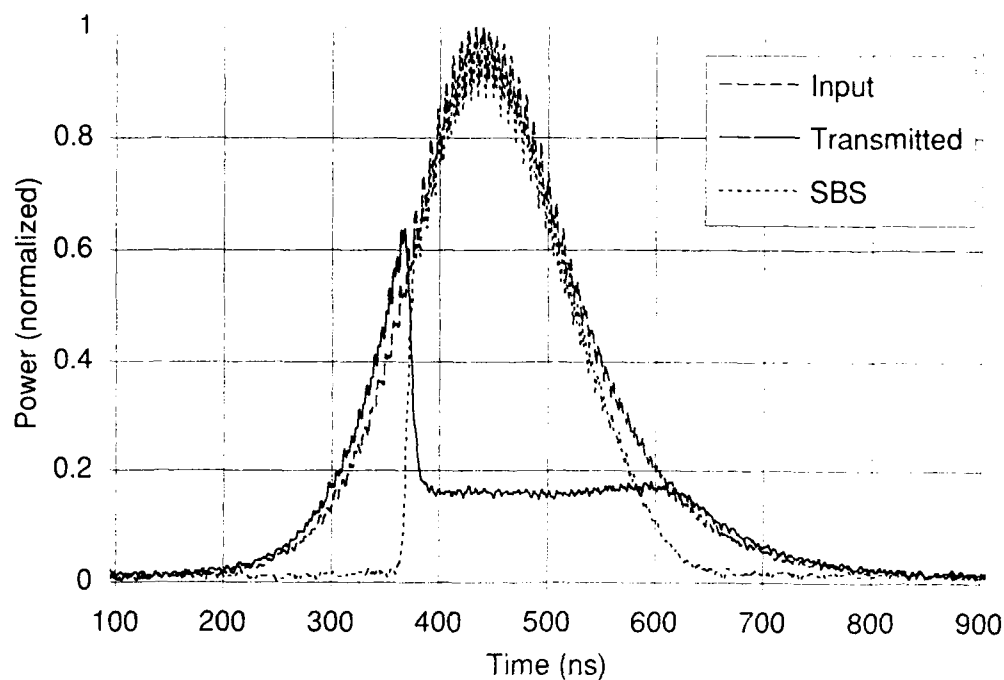


Fig. 41 — Input, SBS, and throughput power showing constant transmitted power

The throughput power is a measure of the steady state power threshold. This is plotted in Fig. 42 and compared with the single- and two-focus SBS thresholds. This shows that the ring reduces the threshold by typically a factor 3 compared with two-focus SBS.

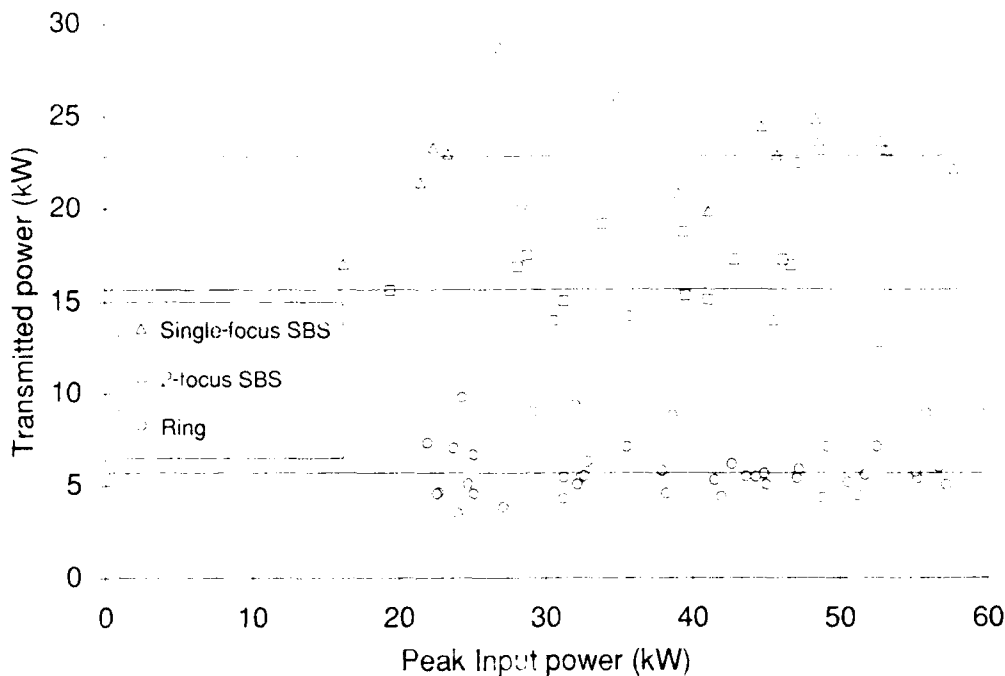


Fig. 42 — Transmitted power as a function of peak input power

We note that the large fluctuations made it difficult to accurately align the ring with the degree of accuracy observed by workers at TRW, although we had been able to get the necessary accuracy in alignment routinely when using the loop geometry.

Figure 43 shows the shot-to-shot variation in the threshold power as a function of time. The maximum threshold is a factor 3 greater than the minimum.

The onset energy is defined in the same way as for the loop scheme. This is plotted in Fig. 44 where it is compared with the onset energy for single- focus and two-focus SBS. It is comparable with the loop onset threshold plotted in Fig. 24.

We attempted to determine whether the fluctuations in Fig. 41 were due to changes in the spectrum of the laser. The throughput power was measured as a function of input power when the laser was operated in three different ways to vary its spectral properties. It was first operated just above threshold, then operated well above threshold, and finally operated with the acousto-optic modulator set to allow some degree of pre-lase, a feature that tends to reduce the spectral bandwidth. These steps had no influence on the statistics of the SBS output; they supported the hypothesis that the fluctuations were due to the Brillouin interaction rather than a variation in the lasers spectrum. The data of Fig. 45 show a clear minimum threshold power of 3 kW and a large spread with the maximum threshold a factor 3 larger than this.

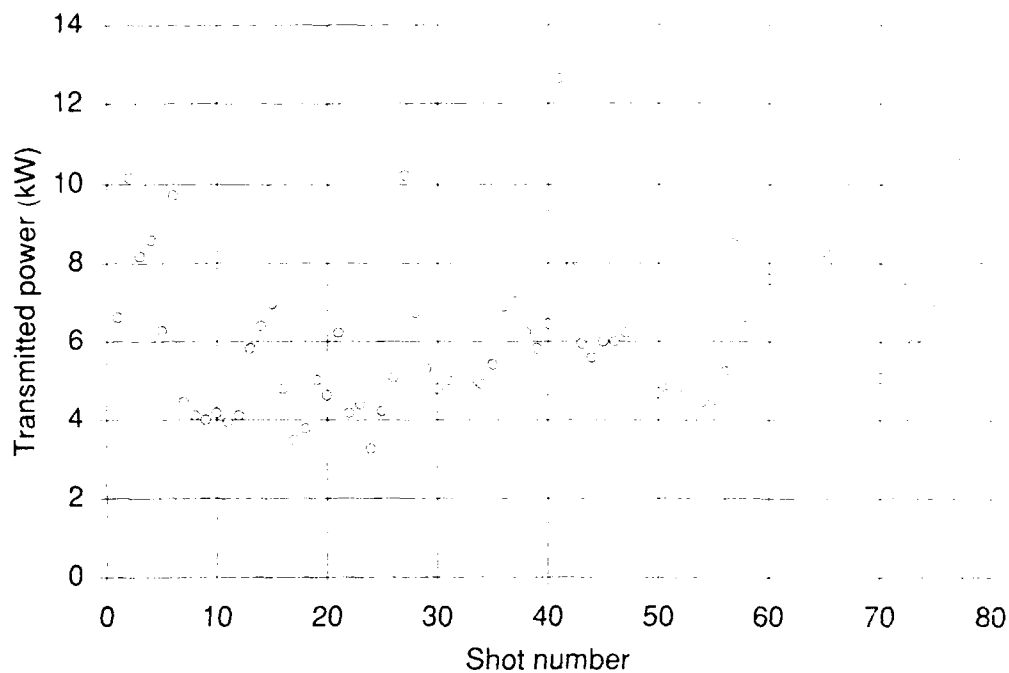


Fig. 43 — Power transmitted through ring measured in consecutive shots showing the shot-to-shot variation

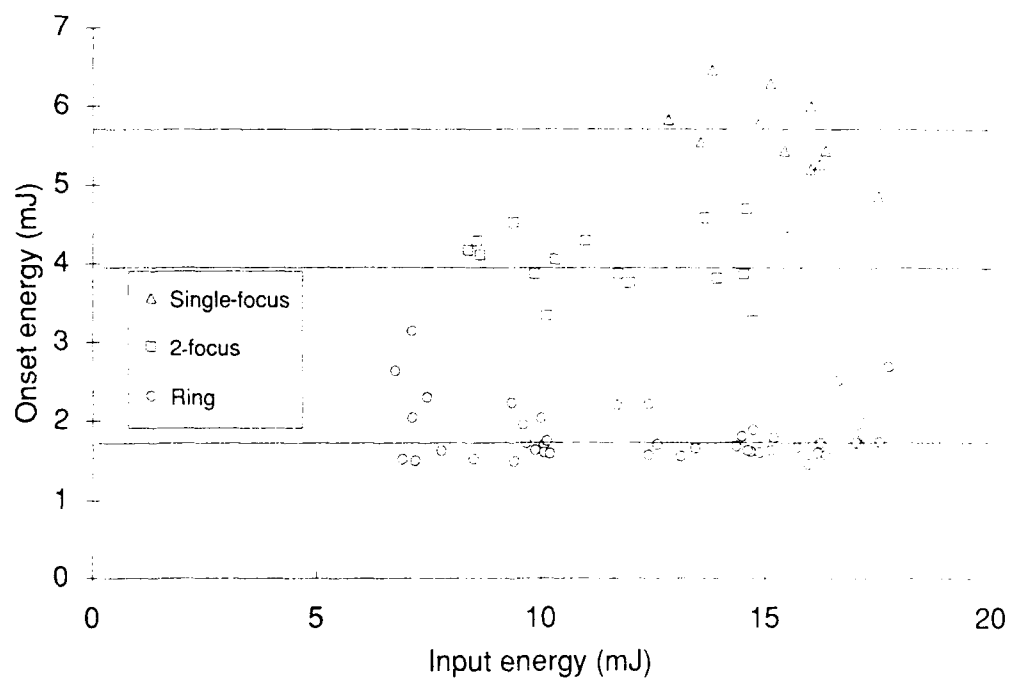


Fig. 44 — Measured onset energy as defined in Fig. 23

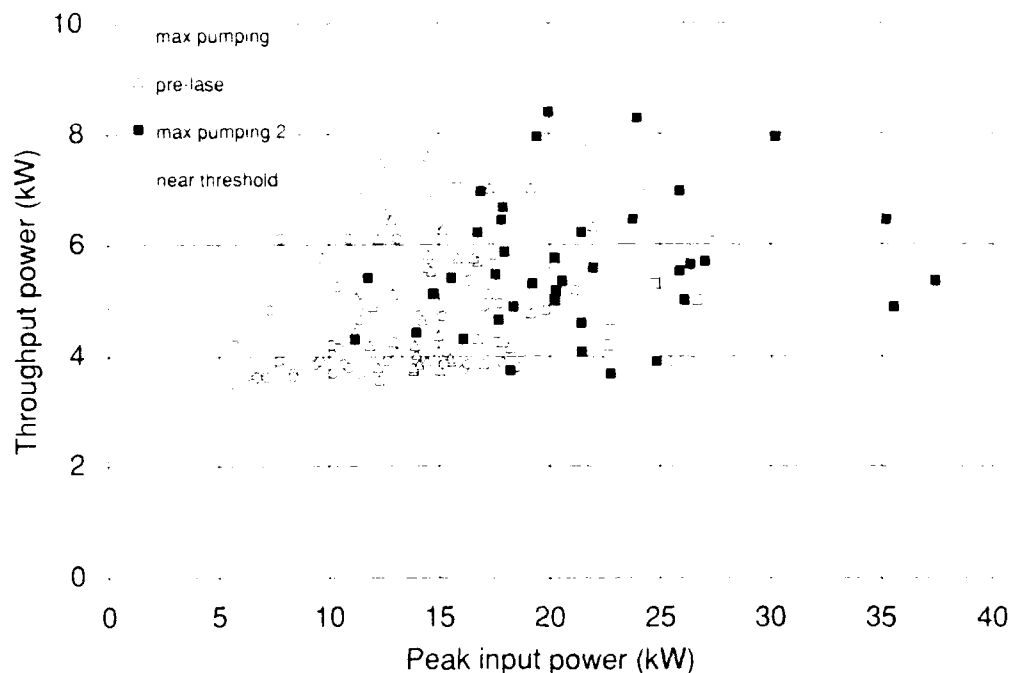


Fig. 45 — Throughput power plotted vs peak input power. Different symbols indicate the laser being operated in different ways to influence the laser spectrum. Apart from a change in the resulting laser power, there was no apparent influence in the statistics of the SBS process.

When the ring was varied in length by scanning mirror 2 over 5 cm, there was no apparent change in the dynamics of the ring, unlike the case of the loop where the modulation was observed at certain critical lengths. Similarly, when the lens after the SBS cell was translated along the axis of the beam, there was no systematic variation in the systems performance.

In addition to variations in the threshold power, there was some variation in the pulse shapes. Occasionally, rapid modulation was observed, as shown in Fig. 46.

The beam quality was also studied. As with the loop scheme, a series of measurements were made of the input and the SBS beam in the near and far fields. The input beam had a near-diffraction-limited Gaussian beam in both near and far field. It also had a near-field waist of 0.38 cm and a far-field divergence of 0.95 mrad, corresponding to 1.4 times the diffraction limit. When this was directed into the ring, the Brillouin output had a Gaussian profile in near and far fields with a near-field waist of 0.39 cm and a divergence of 0.97 mrad. When an aberrator was placed in front of the ring, the transmitted beam broke up into a complex speckle pattern. If the aberrator was double passed using a conventional mirror, the resulting beam had a divergence of 4 mrad. When the ring was operated, the output had a non-Gaussian near-field distribution and a far-field distribution that consisted of 80% of the energy in a near-diffraction-limited Gaussian profile, and the remaining energy in a more highly diverging distribution. In this respect it was very similar to the output characteristics of the loop, and it was not possible to discriminate between the fidelity of the two methods. Figures 47 and 48 show the output distributions of the near and far fields.

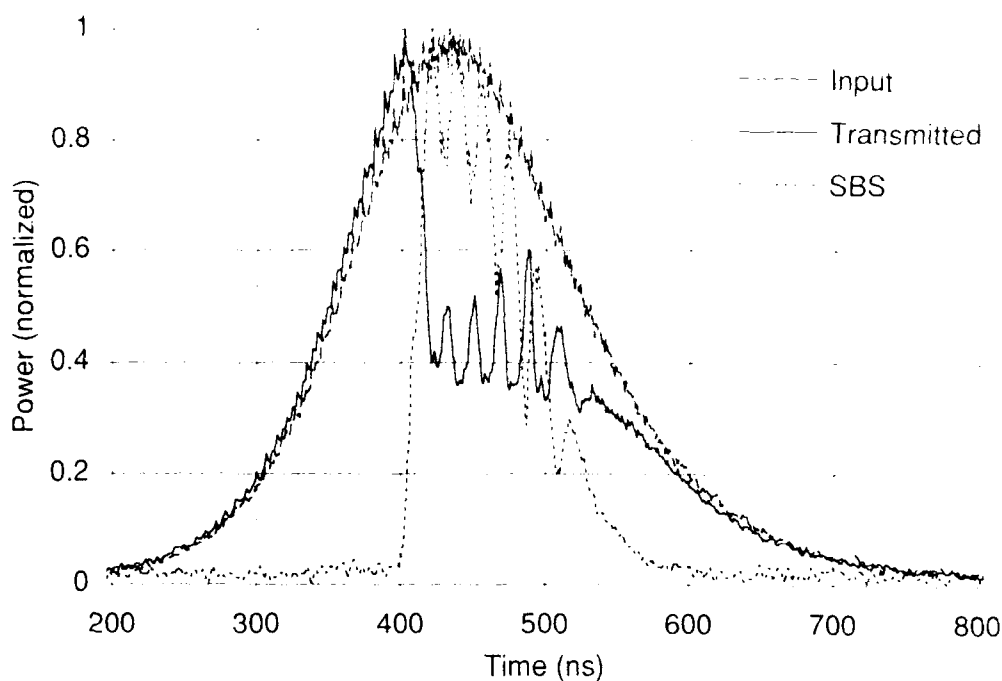


Fig. 46 — Temporal profile observed on some occasions. There were no recorded differences in the conditions for which the above were observed and the conditions for Fig. 41.

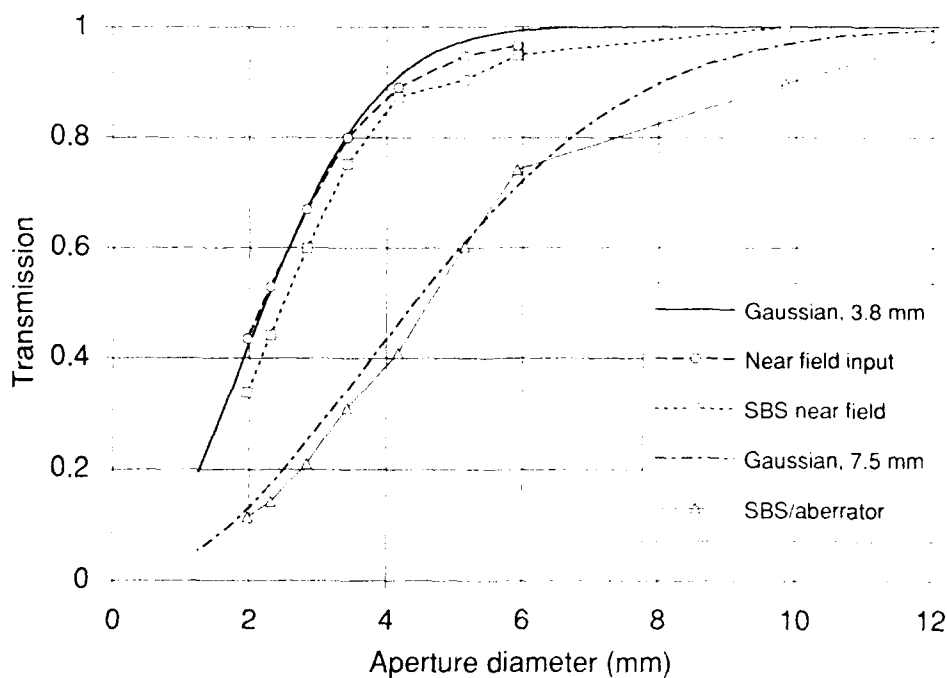


Fig. 47 — Near-field beam energy in bucket data for input and SBS for ring geometry

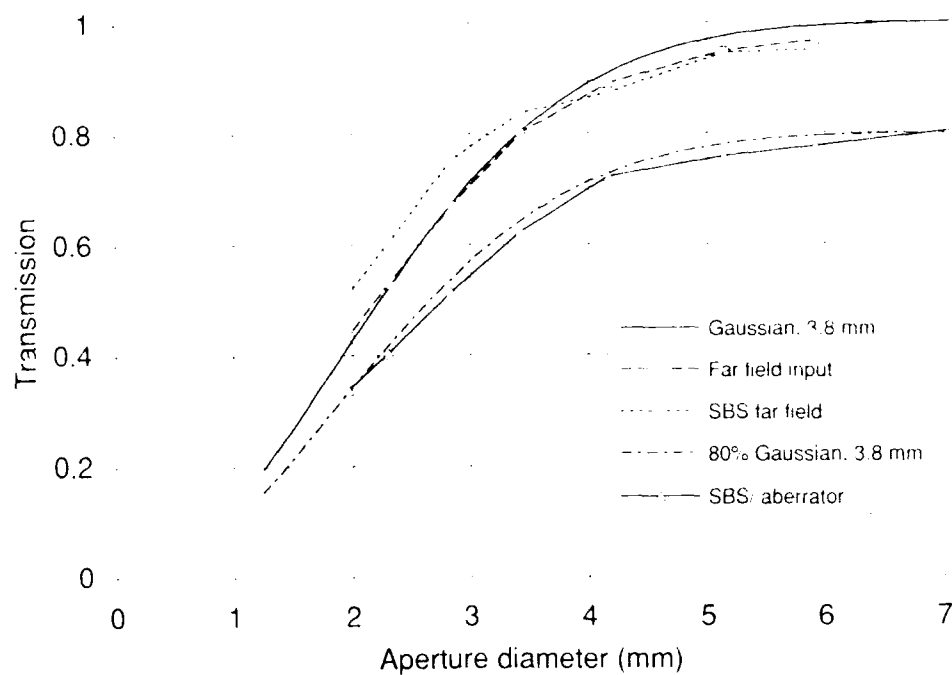


Fig. 48 — Far-field profile data for input and SBS beams using ring geometry

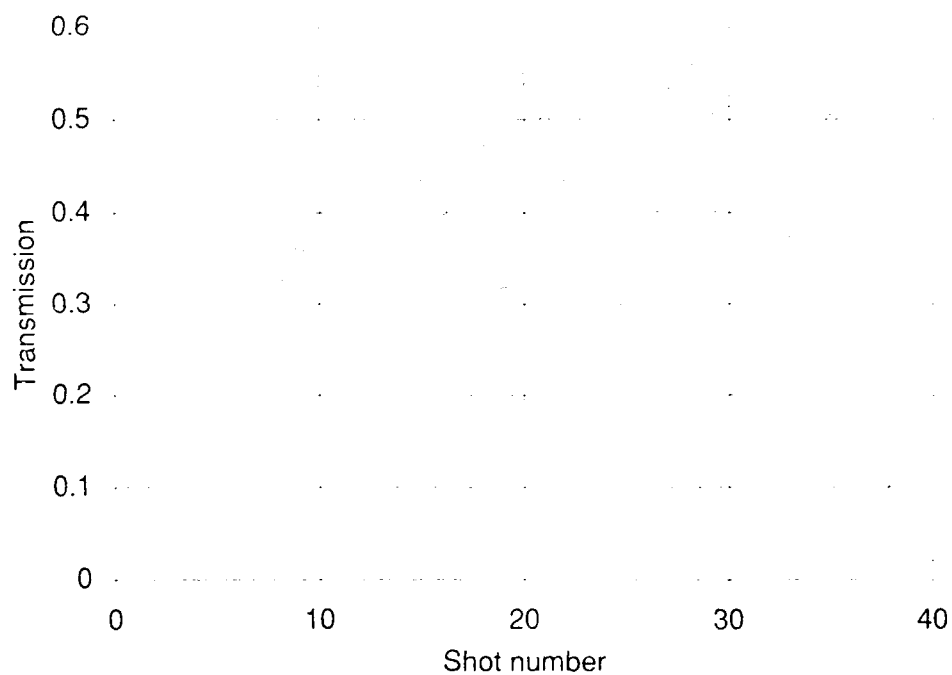


Fig. 49 — Transmission of the SBS beam through a 2.3-mm-diameter pinhole vs shot number; this is closely correlated with the fidelity of the SBS beam.

Finally we studied the fidelity of the ring system on a shot by shot basis. The laser was directed into the ring. The SBS output was returned to a beamsplitter where part was directed onto a monitor and part was directed through a 2.3-mm diameter pinhole. Figure 49 is a sample of the data. The fraction transmitted was recorded and was found to fluctuate, with a maximum transmission of more than 50% observed in approximately 60% of occasions. On some occasions however, the transmission (i.e., fidelity) dropped to below 30%. These results were obtained on the last few days of the experiment, which prevented us from investigating how this fluctuation correlated with the fluctuation in the SBS reflectivity.

## CONCLUSIONS

We have obtained SBS in CS<sub>2</sub> by using a frequency-narrowed Cr,Tm,Ho:YAG laser operating at 2.12  $\mu$ m. Both single-focus SBS and threshold reduction by using a loop and ring have been demonstrated.

A theory of the threshold reduction schemes was developed that described their transient and steady state behavior. The systems were first described as a set of overlapping Gaussian beams, and correction factors were calculated to map the problem onto a one-dimensional model that assumed uniform pump beams.

The theoretical analysis for the two schemes shows that they are each characterized by an initial transient "instability" regime. In this regime the conjugate beam grows exponentially in time, followed by a steady state regime where the conjugate intensity depends only on the pump intensity. In the transient regime the growth rate is approximately proportional to the pump intensity, and the conjugate beam reaches an observable intensity when the total growth has reached a value of  $\exp(25)$ . This occurs when the integrated pump energy reaches some fixed value, which we have called the "onset energy." This onset energy is approximately independent of how far the pump pulse exceeds the threshold. This was observed experimentally.

The theoretical steady state reflectivity grows rapidly from zero as the input power starts to exceed the instability threshold. It then increases in proportion to the input power at higher pump powers. The slope efficiency tends to 100% and theoretically exceeds 100% close to threshold. Thus if the reflectivity is measured at high pump powers and linearly extrapolated back to determine the threshold, the result will be lower than actual instability threshold (see, e.g., Fig. 14).

Considering first the loop scheme, it was found that one key parameter was the phase shift around the loop  $\Delta k \Delta L$ , which needs to be a multiple of  $2\pi$  to produce a conjugate with a low threshold and smooth temporal profile. When this condition was not met, the conjugate and transmitted beams were heavily modulated.

The experimental results agreed well with theory in terms of the onset threshold and the degree of threshold reduction, which typically was 2.2. One noticeable difference between the loop and conventional SBS was that the conventional SBS was strongly modulated, presumably resulting from fluctuations in the initiating noise. In the loop scheme, noise is required to start the process but it is not required once the process starts.

The ring geometry was found to have almost a factor 2 greater threshold reduction than the loop, in agreement with the theory. Unlike the loop geometry, the ring was found to suffer from large shot-to-shot fluctuations in the reflectivity and the fidelity. This was consistent with the theory, which showed that the

loop would be stable provided the loop length varied by less than a few cm from shot to shot. However, the ring length needed to be held constant to within one micron to have the same stability in reflectivity.

This sensitivity to variations in length has not been observed by other researchers. One possible explanation for this is that the ring can also be considered to be a special case of a loop, and in this case the length sensitivity disappears. This can be expected to happen if losses or aberrations change the eigenmodes of the ring cavity to have a somewhat larger mode volume, so that the ring cavity has its ring SBS threshold raised to exceed the threshold it has as a degenerate loop.

## REFERENCES

1. B. Ya. Zel'dovich, N. F. Pilipetsky, and V. V. Shkunov, *Principles of Phase Conjugation* (Springer-Verlag, Berlin, 1985).
2. I. Yu. Anikeev, D. A. Glazov, A. A. Gordeev, I. G. Zubarev, A. B. Mironov, and S. I. Mikhailov, "The Structure of the Stokes Fields Reflected in SBS in a Light Guide," *IEEE J. Quantum Electron*, **25**, 414 (1989).
3. J. Munch, R. F. Wuerker, and M. J. LeFebvre, "Interaction Length for Optical Phase Conjugation by Stimulated Brillouin Scattering: An Experimental Investigation," *Appl. Opt.* **28**, 3099 (1989).
4. M. T. Duignan, B. J. Feldman, and W. T. Whitney, "Threshold Reduction for Stimulated Brillouin Scattering Using a Multipass Herriott Cell," *J. Opt. Soc. Am.* **9**, 548 (1992).
5. M. Cronin-Golomb, B. Fischer, J. O. White, and A. Yariv, "Theory and Applications of Four Wave Mixing in Photorefractive Media," *IEEE J. Quantum Electron* **20**, 12 (1984).
6. A. M. Scott and P. Waggott, "Phase Conjugation by Self-Pumped Brillouin-induced Four-wave Mixing," *Optics Lett*, **12**, 835 (1987).
7. K. D. Ridley and A. M. Scott, "Comparison Between Theory and Experiment in Self-Pumped Brillouin Enhanced Four-Wave Mixing," *J. Opt. Soc. Am. B* **6**, 1701 (1989).
8. D. E. Watkins, K. D. Ridley, and A. M. Scott, "Self-pumped Four-Wave Mixing Using Forward and Backward Brillouin Scattering," *J. Opt. Soc. Am. B* **6**, 1693 (1989).
9. V. I. Odintsov and L. F. Rogacheva, "Efficient Phase Conjugation Under Parametric-feedback Conditions," *Sov. Phys. JETP Lett.* **36**, 344 (1982).
10. G. K. N. Wong and M. J. Damzen, "Investigations of Optical Feedback Used to Enhance Stimulated Scattering," *IEEE J. Quantum Electron*, **26**, 139 (1990).
11. I. M. Bel'dyugin, B. Ya. Zel'dovich, M. V. Zolotarev, and V. V. Shkunov, "Lasers with Wavefront-reversing Mirrors (Review)," *Sov. J. Quantum Electron.* **15**, 1583 (1985).
12. O. P. Zaskal'ko, A. A. Zozulya, and N. N. Panaioti, "Self-reversal of a Light Beam in a Mode of Parametric Generation of Stimulated Mandel'shtam-Brillouin Scattering," *Kratk. Soobsh. po Fiz* **8** (1986).



13. I. Yu. Anikeev, I. G. Zubarev, and S. I. Mikhailov, "Structure of Fields in Self-pumped Stimulated Brillouin Scattering Lasers," *Sov. J. Quantum Electron.* **16**, 1529 (1986).
14. A. A. Zozulya, V. P. Silin, and V. T. Tikhonchuk, "The Theory of Phase Conjugation during Stimulated Scattering in a Self-Intersecting Light Beam," *Sov. Phys. JETP* **65**, 443 (1987).
15. A. A. Zozulya, "Double Phase Conjugate Mirror Is Not an Oscillator," *Opt. Lett.* **16**, 545 (1991).
16. A. A. Esayan, A. A. Zozulya, and V. T. Tikhonchuk, "Influence of Feedback Loop Characteristics on the Field Structure in a Phase-conjugating Ring Mirror," *Sov. J. Quantum Electron.* **21**, 1082 (1991).
17. V. V. Eliseev, N. N. Zhukov, and O. P. Zaskal'ko, "Self-reversal in Parametric Mandel'shtam-Brillouin Lasing," *Izvest. Akad. Nauk SSSR, Ser. Fiz.* **52**, 393-395 (p. 157-160) (1988).
18. I. Yu. Anikeev, D. A. Glazov, I. G. Zubarev, and S. I. Mikhailov, "Stimulated Emission in a Loop Stimulated Brillouin Scattering Laser with a Variable Resonator Length," *Sov. J. Quantum Electron.* **22**, 216 (1992).
19. M. G. Zhanuzakov, A. A. Zozulya, and V. T. Tikhonchuk, "Nonlinear Theory of a Self-reversing Ring Stimulated Brillouin Scattering Mirror," *Sov. J. Quantum Electron.* **19**, 254 (1989).
20. M. G. Zhanuzakov, A. A. Zozulya, and V. T. Tikhonchuk, "Stability of Steady State Stimulated Scattering in a Non-linear Ring Resonator," *Sov. J. Quantum Electron.* **19**, 1445 (1989).
21. N. E. Andreev, A. I. Zykov, and V. T. Tikhonchuk, "Dynamics of Stimulated Brillouin Scattering in an Optical Oscillator with Feedback," *Sov. J. Quantum Electron.* **21**, 1231 (1991).
22. N. E. Andreev, A. I. Zykov, and V. T. Tikhonchuk, "The Dynamics of Light Waves in a Parametric Ring Stimulated Mandel'shtam-Brillouin Scattering Generator," *Kratk. Soob. po Fiz.* **6**, 48-50 (63-67) (1989).
23. D. A. Nikolaev and V. I. Odintsov, "Phase Conjugation Due to Stimulated Brillouin Scattering in a Loop System with a Mirror," *Sov. J. Quantum Electron.* **19**, 1209 (1989).
24. V. V. Eliseev and V. T. Tikhonchuk, "Structure of the Wave Fields in a Non-degenerate parametric Ring Oscillator," *Sov. J. Quantum Electron.* **19**, 751 (1989).
25. V. T. Tikhonchuk and A. A. Zozulya, "Structure of Light Beams in Self-pumped Four-wave Mixing Geometries for Phase Conjugation and Mutual Conjugation," *Prog. Quantum Electron.* **15**, 231 (1992).
26. S. A. Shakir, "Increasing the Efficiency of Stimulated Scattering Phase Conjugate Mirrors," *Proc. SPIE* **540**, 303 (1985).
27. A. M. Scott and K. D. Ridley, "A Review of Brillouin-enhanced Four Wave Mixing," *IEEE J. Quantum Electron.* **25**, 438 (1989).

28. R. M. S. Mengir, J. J. Ottusch, D. C. Jones, and D. A. Rockwell, "Time-resolved Measurements of Stimulated Brillouin Scattering Phase Jumps," *Phys. Rev. Lett.* **68**, 1702 (1992).
29. A. E. Siegman, *Lasers* (University Science Books, Mill Valley, CA, 1986).
30. S. Pfeifer, R. Johnson, and W. Carrion, "Experimental Investigation of Threshold Reduction Techniques in Stimulated Brillouin Scattering," Paper CMG3, Conference on Lasers and Electro-Optics, Technical Digest Series 10 (Optical Society of America, Washington, D.C., 1991) p. 50.